Article

Developmental Cell

α-tubulin tail modifications regulate microtubule stability through selective effector recruitment, not changes in intrinsic polymer dynamics

Graphical abstract

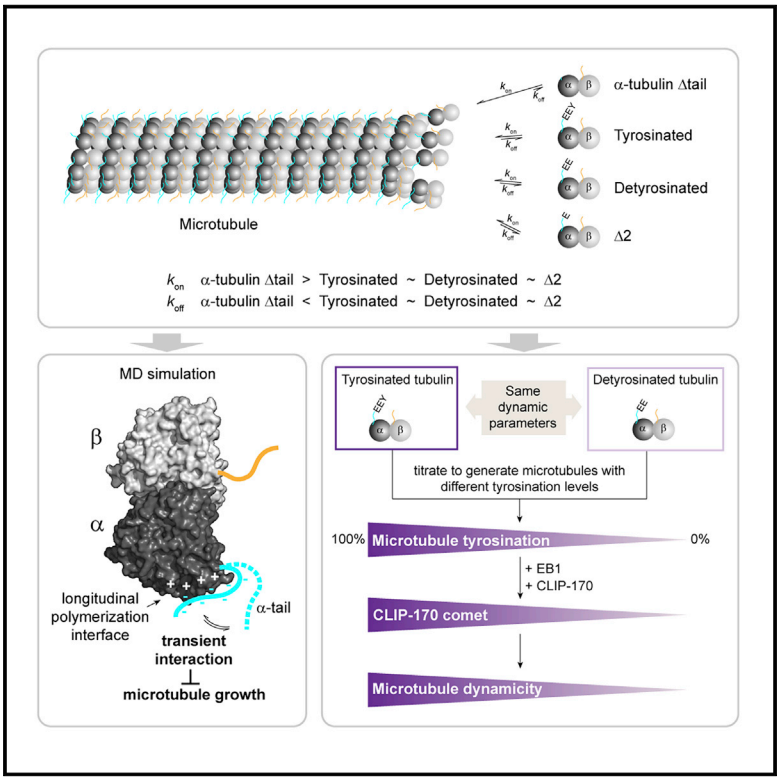

Highlights

- The α-tubulin tail inhibits microtubule growth by occluding a polymerization interface
- The dynamics of tyrosinated, detyrosinated, and Δ2 microtubules are similar
- Tyrosination quantitatively tunes the recruitment of CLIP-170 to the microtubule
- Tyrosination-dependent factor recruitment creates dynamic microtubules subpopulations

Authors

Jiayi Chen, Ekaterina Kholina, Agnieszka Szyk, Vladimir A. Fedorov, Ilya Kovalenko, Nikita Gudimchuk, Antonina Roll-Mecak

Correspondence

nikita_gb@mail.ru (N.G.), antonina@mail.nih.gov (A.R.-M.)

In brief

Microtubules functionalized with different posttranslational modifications have different stabilities in cells. Chen et al. show that tyrosinated, detyrosinated, and Δ2 microtubules have the same dynamic parameters and that their different dynamicity in cells results from the tyrosination-dependent recruitment of CLIP-170.

Chen et al., 2021, Developmental Cell *56*, 2016–2028
July 26, 2021
https://doi.org/10.1016/j.devcel.2021.05.005

CellPress

CellPress

Developmental Cell

Article

α-tubulin tail modifications regulate microtubule stability through selective effector recruitment, not changes in intrinsic polymer dynamics

Jiayi Chen,[1] Ekaterina Kholina,[2] Agnieszka Szyk,[1] Vladimir A. Fedorov,[2,6] Ilya Kovalenko,[2,3,4] Nikita Gudimchuk,[5,6,7,*] and Antonina Roll-Mecak[1,8,9,*]

[1]Cell Biology and Biophysics Unit, National Institute of Neurological Disorders and Stroke, Bethesda, MD 20892, USA
[2]Department of Biology, Lomonosov Moscow State University, Moscow, Russia
[3]Astrakhan State University, Astrakhan 414056, Russia
[4]Sechenov University, Moscow 119991, Russia
[5]Department of Physics, Lomonosov Moscow State University, Moscow, Russia
[6]Center for Theoretical Problems of Physicochemical Pharmacology, Russian Academy of Sciences, Moscow, Russia
[7]Dmitry Rogachev National Research Center of Pediatric Hematology, Oncology and Immunology, Moscow, Russia
[8]Biochemistry and Biophysics Center, National Heart Lung and Blood Institute, Bethesda, MD 20892, USA
[9]Lead contact
*Correspondence: nikita_gb@mail.ru (N.G.), antonina@mail.nih.gov (A.R.-M.)
https://doi.org/10.1016/j.devcel.2021.05.005

SUMMARY

Microtubules are non-covalent polymers of αβ-tubulin dimers. Posttranslational processing of the intrinsically disordered C-terminal α-tubulin tail produces detyrosinated and Δ2-tubulin. Although these are widely employed as proxies for stable cellular microtubules, their effect (and of the α-tail) on microtubule dynamics remains uncharacterized. Using recombinant, engineered human tubulins, we now find that neither detyrosinated nor Δ2-tubulin affect microtubule dynamics, while the α-tubulin tail is an inhibitor of microtubule growth. Consistent with the latter, molecular dynamics simulations show the α-tubulin tail transiently occluding the longitudinal microtubule polymerization interface. The marked differential *in vivo* stabilities of the modified microtubule subpopulations, therefore, must result exclusively from selective effector recruitment. We find that tyrosination quantitatively tunes CLIP-170 density at the growing plus end and that CLIP170 and EB1 synergize to selectively upregulate the dynamicity of tyrosinated microtubules. Modification-dependent recruitment of regulators thereby results in microtubule subpopulations with distinct dynamics, a tenet of the tubulin code hypothesis.

INTRODUCTION

Microtubules are mesoscopic non-covalent polymers built from αβ-tubulin heterodimers. They switch stochastically between polymerization and depolymerization, a phenomenon known as dynamic instability (Walker et al., 1988; Horio and Hotani, 1986; Mitchison and Kirschner, 1984). The transition from growth to depolymerization is called catastrophe and the transition from depolymerization state to growth is called rescue. Dynamic instability is essential for chromosome segregation, cellular motility, and differentiation (Kirschner and Mitchison, 1986). Many cellular factors modulate microtubule polymerization and depolymerization. The last two decades have seen an explosion in our understanding of their mechanism of action (reviewed in Alfaro-Aco and Petry, 2015; Akhmanova and Steinmetz, 2010a). However, our understanding of the relationship between the diversity of tubulin itself and its dynamic properties lags behind. Microtubules in cells are functionalized through chemically diverse and evolutionarily conserved posttranslational modifications (Janke and Magiera, 2020; Roll-Mecak, 2020; Verhey and Gaertig, 2007). The majority of these modifications concentrate on the C-terminal tails of the αβ-tubulin heterodimer. These are intrinsically disordered elements that project from the compact, folded globular core of the tubulin dimer and form a negatively charged dense brush on the microtubule surface. The effects of tubulin tail modifications on microtubule dynamics are unknown, even though these modifications have been widely used for decades as surrogates for microtubule stability in cellular studies where the dynamics of microtubule subpopulations are inferred from their posttranslational modification status detected with specific antibodies.

Some of the most widely used proxies for microtubule stability in cells are detyrosination and tyrosination, for stable and dynamic microtubules, respectively. Detyrosination and tyrosination involve the removal and addition of the terminal tyrosine on α-tubulin, respectively. Tyrosination was the first tubulin

posttranslational modification discovered (Barra et al., 1973). The terminal tyrosine is removed by carboxypeptidases vasohibins/SVBP (Aillaud et al., 2017; Nieuwenhuis et al., 2017) and added back by tubulin tyrosine ligase (Flavin and Murofushi, 1984; Argaraña et al., 1978; Raybin and Flavin, 1977; Barra et al., 1973) as part of this detyrosination/tyrosination cycle. In certain cell types, most prominently in neurons, a large portion of the detyrosinated α-tubulin pool proceeds to a second modification step which involves the removal of the penultimate glutamate in the α-tail resulting in Δ2-tubulin (Paturle-Lafanechère et al., 1994, 1991). Approximately 35% of brain tubulin is in this state (Paturle-Lafanechère et al., 1994). This modification is also associated with stable microtubule populations (Paturle-Lafanechère et al., 1994). Unlike detyrosination, which can be reversed by tubulin tyrosine ligase, the Δ2 modification is irreversible and thus removes this tubulin variant from the detyrosination/tyrosination cycle (Paturle-Lafanechère et al., 1991). These posttranslational modifications are spatially and temporally regulated and are important in a wide array of biological processes ranging from cell division (Akera et al., 2017; Iwata-Otsubo et al., 2017; Barisic et al., 2015; Peris et al., 2006) to neurogenesis (Aillaud et al., 2017; Erck et al., 2005), myogenesis (Chang et al., 2002; Gundersen et al., 1989), and cardiomyocyte function (Robison et al., 2016) (reviewed in Roll-Mecak, 2019). For example, microtubules that orient in the direction of cell migration are enriched in detyrosinated tubulin (Gundersen and Bulinski, 1988); kinetochore microtubules are also enriched in detyrosinated tubulin, whereas astral microtubules are enriched in tyrosinated tubulin (Gundersen and Bulinski, 1986a). Stable microtubules in axons and cilia are enriched in Δ2 (Paturle-Lafanechère et al., 1994) and detyrosinated tubulin (Gundersen and Bulinski, 1986b), while the dynamic microtubules in growth cones are mostly tyrosinated (Marcos et al., 2009; Witte et al., 2008; Robson and Burgoyne, 1989). The presence or absence of the C-terminal tyrosine on α-tubulin recruits microtubule effectors. For example, the microtubule tip-binding protein CLIP-170 (Bieling et al., 2008; Peris et al., 2006), the depolymerizing kinesin-13 MCAK (Sirajuddin et al., 2014; Peris et al., 2009), and dynactin (McKenney et al., 2016; Nirschl et al., 2016; Peris et al., 2006) associate preferentially with tyrosinated microtubules, while the CENP-E motor prefers detyrosinated microtubules (Barisic et al., 2015) and detyrosination mediates the interaction between microtubules and intermediate filaments (Kreitzer et al., 1999).

Pioneering work by several laboratories showed that, in cells, microtubules with slow turnover ($t_{1/2} \sim$ tens of minutes to hours) and those resistant to cold or pharmacologically induced depolymerization are enriched in detyrosinated and Δ2-tubulin, whereas dynamic microtubules that turn over rapidly ($t_{1/2} \sim$ 2–5 min) are enriched in tyrosination (Webster and Borisy, 1989; Kreis, 1987; Schulze and Kirschner, 1987; Webster et al., 1987b). Since then, cell biologists use antibodies against these modifications to distinguish between "stable" and "dynamic" microtubules in cells (Xu et al., 2011; Whipple et al., 2010; Shintani et al., 2009; Infante et al., 2000; Webster and Borisy, 1989; Kreis, 1987; Schulze and Kirschner, 1987; Webster et al., 1987a). In fact, this has become almost the *de facto* tool for distinguishing between these two subpopulations of microtubules in cells. However, we still do not know the answer to the fundamental question: how do these modifications affect microtubule dynamics? Do they impact microtubule dynamics directly or do they recruit regulators that impact their dynamics *in trans*? Kirschner and colleagues speculated that the selective recruitment of hypothetical factors to the detyrosinated microtubule could further stabilize it as part of a positive feedback loop (Schulze and Kirschner, 1987). The effect of posttranslational modifications on polymer dynamics has remained an unsolved problem in the field for more than three decades because of the inability to make well-defined preparations of unmodified and differentially modified tubulin for *in vitro* reconstitution assays.

An early clue to the effects of the detyrosination/tyrosination cycle came from cellular work that examined the stability of microtubules in detergent-extracted cells that were treated with carboxypeptidase, which non-specifically removes C-terminal amino acids (Khawaja et al., 1988). These experiments showed that tyrosinated and detyrosinated microtubules respond similarly to nocadozole treatment as well as dilution. However, these studies did not examine microtubule dynamics. Microtubule dynamics parameters of pure tyrosinated, detyrosinated, or Δ2-tubulin microtubules have yet to be reported. This gap in our knowledge of the dynamic parameters of different types of tubulins stems from the fact that biochemical investigations into microtubule functions have relied in the last four decades on tubulin purified from brain tissue. While tubulin from this source is easily isolated and abundant (Weisenberg, 1972), it is highly heterogeneous as it is abundantly and diversely posttranslationally modified. Thus, this tubulin is not appropriate for understanding the individual contributions of posttranslational modifications to microtubule functions. Recent successes with the expression and purification of single tubulin isotypes recombinantly (Ti et al., 2018; Vemu et al., 2016; Minoura et al., 2013) enable us to explore the relationship between tubulin sequence, structure, and dynamics and establish whether and how tubulin modifications regulate intrinsic polymer properties.

Here, we use recombinant homogeneous and isotypically pure α1A/βIII tubulin to understand the role of the α-tubulin tail and its modifications in regulating microtubule dynamics. Combining *in vitro* microtubule dynamics assays and molecular dynamics simulations we show that the intrinsically disordered α-tubulin tail negatively regulates microtubule polymerization by transiently interacting with the α-tubulin longitudinal polymerization interface. In contrast, loss of only the ultimate tyrosine (detyrosination) and penultimate glutamate (Δ2 modification) in the α-tubulin tail does not affect microtubule dynamic parameters. However, we show that α-tubulin tyrosination quantitatively tunes the density of CLIP-170 at the microtubule plus end and that CLIP-170 synergizes with EB1 to selectively increase the dynamicity of tyrosinated microtubules. Thus, our work establishes that tyrosinated, detyrosinated and the Δ2 modified microtubules have similar intrinsic dynamic parameters and demonstrates that tyrosination-dependent recruitment of microtubule regulators generates microtubule subpopulations with distinct dynamic properties, laying the foundation for the regulation of microtubule dynamics by the tubulin code in cells.

RESULTS

The intrinsically disordered α-tubulin tail inhibits microtubule growth and dynamicity

The last twelve residues in the α-tubulin tail are intrinsically disordered. The C-terminal tails of tubulin are not resolved in all cryoelectron microscopy microtubule reconstructions to date, including reconstructions of homogeneous single-isotype microtubules (Ti et al., 2018; Vemu et al., 2016). Cryo-EM studies revealed that the C-terminal tails are ordered only when bound to microtubule effectors such as the Ndc80 complex (Alushin et al., 2010) or the tubulin tyrosine ligase-like 7 (TTLL7) glutamylase (Garnham et al., 2015). The proteolytic removal of both α and β-tails lowers the critical concentration for tubulin polymerization, as measured by sedimentation assays, and results in the formation of heterogeneous polymeric structures such as ribbons, sheets, and hooks (Knipling et al., 1999; Serrano et al., 1988; White et al., 1987). However, these experiments relied on the non-specific proteolytic cleavage of both C-terminal tails that yields a heterogeneous sample with varying degrees of tubulin tail removal. Moreover, all these studies used proteases that cleave the β-tail before the α-tail (Bhattacharyya et al., 1985) and thus could not establish the effects of the α-tail alone on microtubule properties. To study the contribution of the α-tubulin tail to microtubule dynamics, we recombinantly expressed and purified wild-type human α1A/βIII tubulin with a native carboxyl terminus (Vemu et al., 2016), and an α1AΔ-tail/βIII tubulin, which misses the last twelve residues of α-tubulin (Figures 1A, S1A, S1B, and S2A; STAR Methods). We then reconstituted microtubule dynamics *in vitro* by nucleating microtubules from GMPCPP-stabilized microtubule seeds and imaged the microtubules by label-free interference reflection microscopy (IRM) (Mahamdeh et al., 2018; Figure 1B). Label-free imaging avoids the confounding effects of fluorescently labeled tubulin on microtubule dynamics (Vigers et al., 1988) and allows data collection with high temporal resolution and minimal photodamage.

We find that tailless α1AΔ-tail/βIII microtubules nucleate from seeds robustly at tubulin concentrations as low as 1 μM. Consistent with this, the critical concentration for the α-tailless tubulin is 0.04 ± 0.04 μM for α1AΔ-tail/βIII versus 0.94 ± 0.18 μM for the α1A/βIII wild-type construct, as determined from a linear regression of the mean growth rates as a function of tubulin concentration (Figure 1C; Oosawa, 1970; STAR Methods). This analysis also shows that the absence of the α-tail increases the apparent tubulin on rate at the plus end by 2.4-fold (8.50 ± 0.12 versus 3.48 ± 0.08 μM^{-1} s^{-1} for α1AΔ-tail/βIII and α1A /βIII microtubules, respectively, Figure 1D) while also decreasing the apparent off rate by almost 10-fold (0.35 ± 0.35 versus 3.20 ± 0.63 s^{-1} for α1AΔ-tail/βIII and α1A/βIII microtubules, respectively, Figure 1D). Thus, α-tailless microtubules grow considerably faster. For example, at 4 μM tubulin, α1AΔ-tail/βIII microtubules grow 2.9-fold faster than wild-type microtubules. This increase in growth rate is accompanied by a decrease in catastrophe rates (Figure 1E). As a result, at 4 μM tubulin, in the absence of the α-tail, microtubules grow almost 6-fold longer before they depolymerize (7.82 ± 0.35 μm versus 1.32 ± 0.07 μm for α1AΔ-tail/βIII and α1A/βIII microtubules, respectively Figure S1C). Rescues are very rare both for α1A/βIII and α1AΔ-tail/βIII microtubules and were thus not quantified, similar to the low rescue rates observed for heterogeneous brain microtubules (Vemu et al., 2016; Walker et al, 1988). Thus, our *in vitro* dynamics microtubule assays reveal that the α-tubulin tail inhibits microtubule growth and promotes catastrophe.

A growing microtubule is protected from depolymerization by a GTP-tubulin cap generated by the faster rate of GTP-tubulin addition to the microtubule end compared with that of GTP hydrolysis after tubulin lattice incorporation (Carlier, 1982; Carlier and Pantaloni, 1981). The microtubule undergoes catastrophe when its GTP-cap erodes (Duellberg et al., 2016). Plotting plus-end catastrophe frequencies against growth rate shows that microtubules catastrophe less frequently when growth rates increase and that they are similar between the wild-type and tailless microtubules at similar growth rates, i.e., at similar rates of GTP-tubulin addition to the growing plus end (Figure 1F). We further refined our investigation into whether catastrophe frequencies are due to differences in the size of the stabilizing GTP-tubulin cap by determining catastrophe frequencies of α1A/βIII and α1AΔ-tail/βIII microtubules with growth rates that matched within less than 10% standard deviation (Figure 1G). This analysis also shows that catastrophe frequencies are statistically indistinguishable (Figure 1H). Thus, the decrease in catastrophe frequency seen with the α-tailless tubulin is due primarily to the differences in the kinetics of tubulin addition at the microtubule end.

The α-tubulin tail interacts transiently with the longitudinal polymerization interface

We hypothesized that the strong attenuation of microtubule growth rates by the α-tubulin tail may be explained by a transient interaction with surfaces on the tubulin dimer involved in polymerization (Figure 2A). Thus, we used all-atom explicit solvent MD simulations of free GTP-tubulins to investigate the dynamics of the intrinsically disordered tubulin tails (Figure S3A). These simulations revealed that the α-tubulin tail interacts transiently with the α-tubulin longitudinal polymerization interface, thus likely directly interfering with its addition to a protofilament in the microtubule (Figure 2B; Video S1). We observe this interaction in all of our five independent 1 μs simulations. The α-tail associates with the longitudinal interface for 83% ± 20% of the simulation time, with as little as 52% in one simulation, but in some 100% of the time. Engagement in relatively long-lasting interactions with the tubulin body explains the variable occlusion durations in our simulations. A metadynamics simulation, in which an extra energy potential is applied to the C terminus of the tail in order to accelerate its dynamics and ensure better sampling of configuration space also revealed an association of the α-tubulin tail with the longitudinal polymerization interface (Figures S4A–S4C). Association of the α-tubulin tail occludes up to 33% of the solvent accessible area of the longitudinal interface (Figure 2C). We mapped the regions on the tubulin body surface with which the α-tail prefers to interact by computing the probabilities of contact between the α-tubulin tail and residues in the tubulin body (Figure 2D). The residues with highest contact probabilities map to the α-tubulin longitudinal polymerization interface (Figures 2D–2F and S4C). The simulations indicate that the interaction with the α-tail is facilitated by multiple contacts with conserved positively charged residues at the interface through the negatively charged glutamates in the α-tail (Figures 2G and S3B). The individual tubulin tail residues have similar

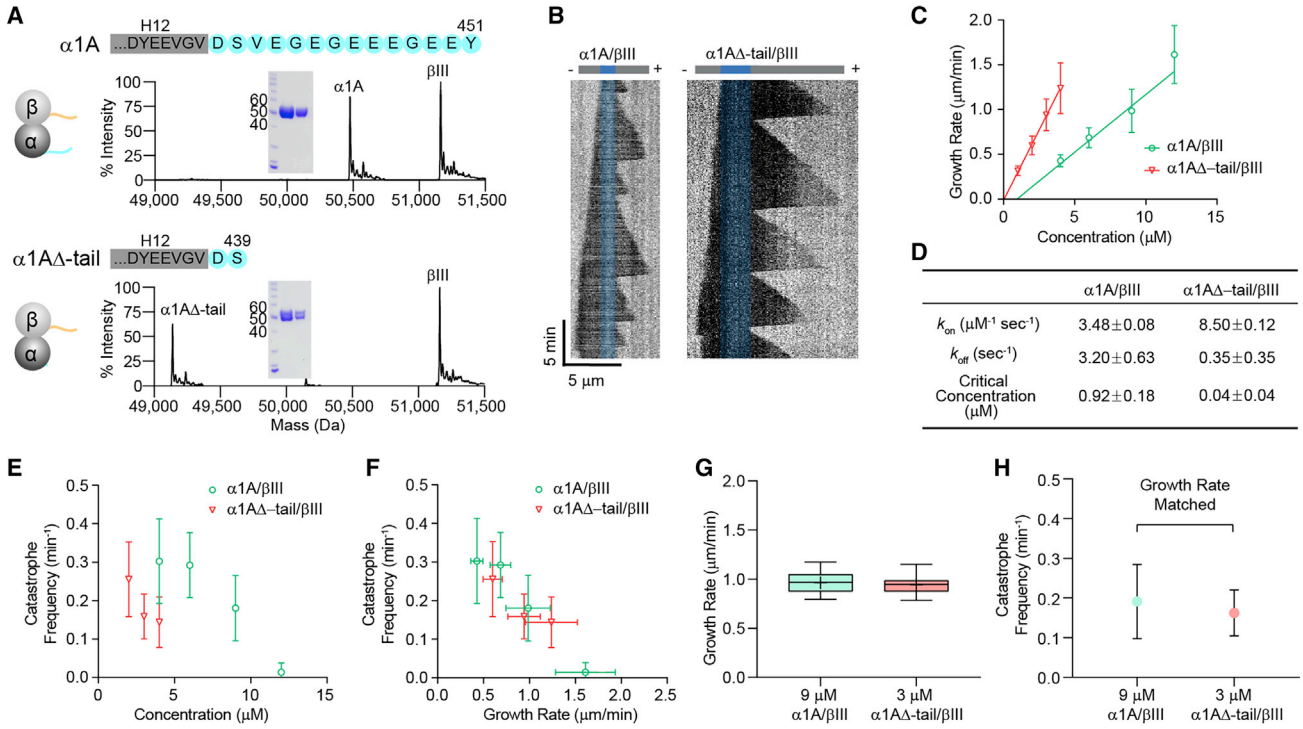

Figure 1. The α-tubulin tail inhibits microtubule polymerization and catastrophe

(A) Mass spectra and SDS-polyacrylamide gel (inset: 5 and 2 μgs of tubulin) of recombinant human α1A/βIII and α1AΔ-tail/βIII tubulin purified to >99% homogeneity (Figures S1A and S1B; STAR Methods). The C-terminal sequences of human α1A and α1AΔ-tail tubulin are shown in cyan. The sequence in the gray rectangle denotes the H12 helix, based on the cryo-EM structure of α1A/βIII microtubules (PDB ID: 5JCO; Vemu et al., 2016).

(B) Representative kymographs showing microtubule growth at 3 μM for α1A/βIII (left) and α1AΔ-tail/βIII (right) microtubules. GMPCPP-stabilized seeds are pseudo-colored in blue.

(C) Plus-end growth rates as a function of tubulin concentration for α1A/βIII and α1AΔ-tail/βIII tubulin. Error bars represent SD (n = 181, 256, 608, and 82 growth phases for α1A/βIII at 4, 6, 9, and 12 μM, respectively; n = 214, 518, 529, and 424 growth phases for α1AΔ-tail/βIII at 1, 2, 3, and 4 μM, respectively).

(D) Tubulin apparent on and off rates at the plus end, and critical concentration determined by fitting a linear regression of the mean growth rates versus tubulin concentration shown in (C); $p < 0.0001$ as determined by the Tukey range test for the differences in k_{on} and k_{off} rates between α1A/βIII and α1AΔ-tail/βIII tubulin.

(E) Microtubule plus-end catastrophe frequencies as a function of tubulin concentration. Error bars represent SD (n = 27, 29, 86, and 59 microtubules for α1A/βIII at 4, 6, 9, 12 μM, respectively; n = 59, 63, 73, 70, and 23 microtubules for α1AΔ-tail/βIII at 2, 3, 4, 6 μM, respectively).

(F) Microtubule plus-end catastrophe frequencies plotted against growth rates. Error bars represent SD (n values as in C and E).

(G) Box-whisker plot of α1A/βIII and α1AΔ-tail/βIII microtubules with matched growth rates within 10% SD (0.96 ± 0.10 μm/min, n = 61 α1A/βIII microtubules at 9 μM; 0.94 ± 0.09 μm/min, n = 59 α1AΔ-tail/βIII microtubules at 3 μM). Whiskers indicate minimum and maximum.

(H) Catastrophe frequencies for growth-rate matched α1A/βIII and α1AΔ-tail/βIII microtubules shown in (G); n = 61 and 59 microtubules for α1A/βIII and α1AΔ-tail/βIII, respectively; error bars represent SD.

contact probabilities with the α-tubulin longitudinal interface (Figure S3C). This suggests that there is not a single, specific residue on the α-tail that nucleates this interaction. The high density of glutamates in the tail is conserved across all α-tubulin isotypes (Figure S2), despite the higher sequence variability in this region compared with the tubulin core. Moreover, the length of the α-tubulin tails is more stringently conserved compared with that of β-tubulin tails (Roll-Mecak, 2015; Ludueña, 2013 and Figure S2), consistent with an evolutionary pressure to maintain important functional interactions.

Tyrosinated, detyrosinated, and Δ2 microtubules have similar dynamics *in vitro*

Cells posttranslationally remove the ultimate and penultimate residues in the α-tubulin tail to generate detyrosinated and Δ2 microtubules, respectively. Detyrosinated and Δ2 microtubules are associated with stable microtubule subpopulations in cells (Paturle-Lafanechère et al., 1994; Webster and Borisy, 1989; Kreis, 1987; Schulze and Kirschner, 1987; Webster et al., 1987b). Since removing the entire intrinsically disordered α-tubulin tail has dramatic effects on microtubule stability, we next examined whether detyrosination and the Δ2 modification also affect intrinsic polymer properties. We performed *in vitro* dynamics assays with recombinantly expressed, homogeneous, and isotypically pure human tyrosinated (α1A/βIII), detyrosinated (α1A-Y/βIII) and Δ2 (α1A-Δ2 /βIII) tubulin (Figures 3A and 3B). Our tagging scheme produces an α-tubulin with a native carboxyl terminus (Vemu et al., 2016; STAR Methods) and thus suitable for examining the effects of the α-tail modification cycle without any confounding effects from a tag. Using our IRM-based *in vitro* dynamics assays we find that detyrosinated (α1A-Y/βIII) and Δ2 (α1A-Δ2/βIII) microtubules have similar growth rates across a range of concentrations (Figure 3C). A linear regression analysis of the growth rates as a function of tubulin concentration

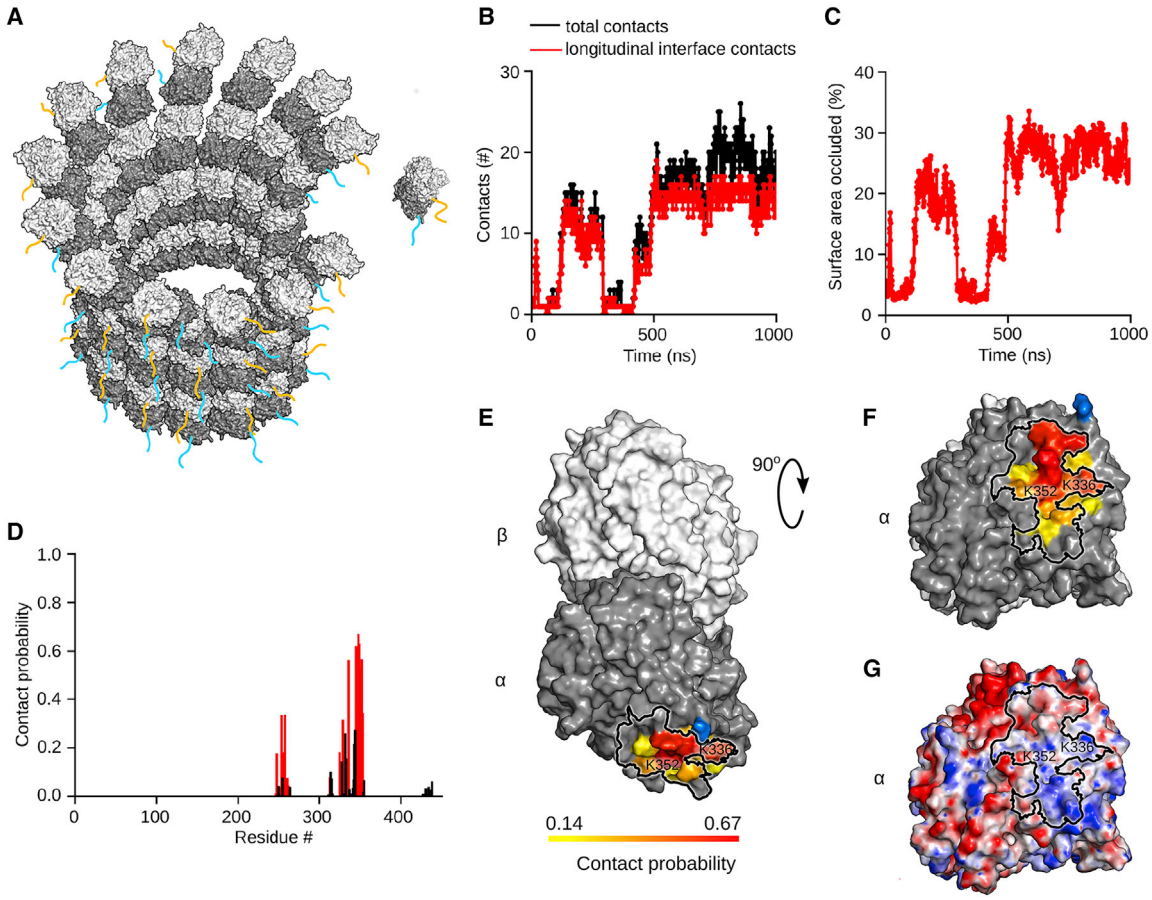

Figure 2. The α-tubulin tail occludes the longitudinal polymerization interface transiently

(A) Schematic of tubulin dimer incorporation into a protofilament at the growing microtubule plus-end. α-tubulin tail, cyan, β-tubulin tail, orange in cartoon representation.

(B) Number of contacts between residues in the tubulin body and the α-tubulin tail as a function of time identified from the MD simulation. Black dots indicate total number of contacts, red dots indicate contacts with the α-tubulin longitudinal polymerization interface.

(C) Percentage of solvent-accessible surface area of the α-tubulin longitudinal interface occluded by the α-tubulin tail in the simulation shown in (B).

(D) Contact probability for residues in the α-tubulin core with the α-tubulin tail based on five independent one-microsecond-long simulation runs (STAR Methods). Red bars correspond to contacts with the α-tubulin polymerization interface; black bars, contacts with the tubulin surface elsewhere.

(E) Molecular surface of the αβ-tubulin dimer colored on a gradient from yellow to red according to the probability of its contact with the α-tubulin tail. Residue S439 where the tail originates is shown in blue.

(F) View of the longitudinal polymerization interface colored as in (E). Black outline delineates the longitudinal polymerization interface.

(G) Electrostatic potential distribution mapped on the surface of the tubulin dimer in the same orientation as in (F). Red and blue colors correspond to negative and positive electrostatic potential values, respectively. Black outline delineates the longitudinal polymerization interface. See also Figures S3 and S4.

yields similar tubulin apparent on and off rates at the plus end for all three tubulin variants (Figure 3D). Both detyrosinated and Δ2-tubulin show a statistically significant but very small increase (11% and 9%, respectively) in their apparent on rates compared with tyrosinated tubulin, consistent with our molecular dynamics simulations, which show that the two terminal tubulin tail residues do not have a dominant contribution to the interaction with the α-tubulin longitudinal interface, having similar contact probabilities as other tail residues (Figure S3C). Our analysis also reveals that tyrosinated, detyrosinated, and Δ2 tubulin have similar critical concentrations for nucleation. Lastly, the three microtubule types also have similar catastrophe frequencies across a range of concentrations (Figure 3E). The speeds at which the three different types of microtubule depolymerize are also statistically indistinguishable (Figures 3F and 3G). In conclusion, our *in vitro* results demonstrate quantitatively that the *in vivo* differences in dynamics between detyrosinated, Δ2, and tyrosinated microtubule subpopulations are exclusively due to the differential recruitment of effectors and not to intrinsic differences in polymer dynamics.

Selective recruitment of CLIP-170 to tyrosinated microtubules increases their dynamicity

One of the tenets of the tubulin code hypothesis is that post-translational modifications tune microtubule dynamics either directly or indirectly, through the recruitment of cellular factors, thus creating microtubule subpopulations with different dynamic properties in cells. We thus wanted to test whether the tyrosination-specific recognition of a cellular effector can selectively regulate microtubule stability. The dynamic behavior of

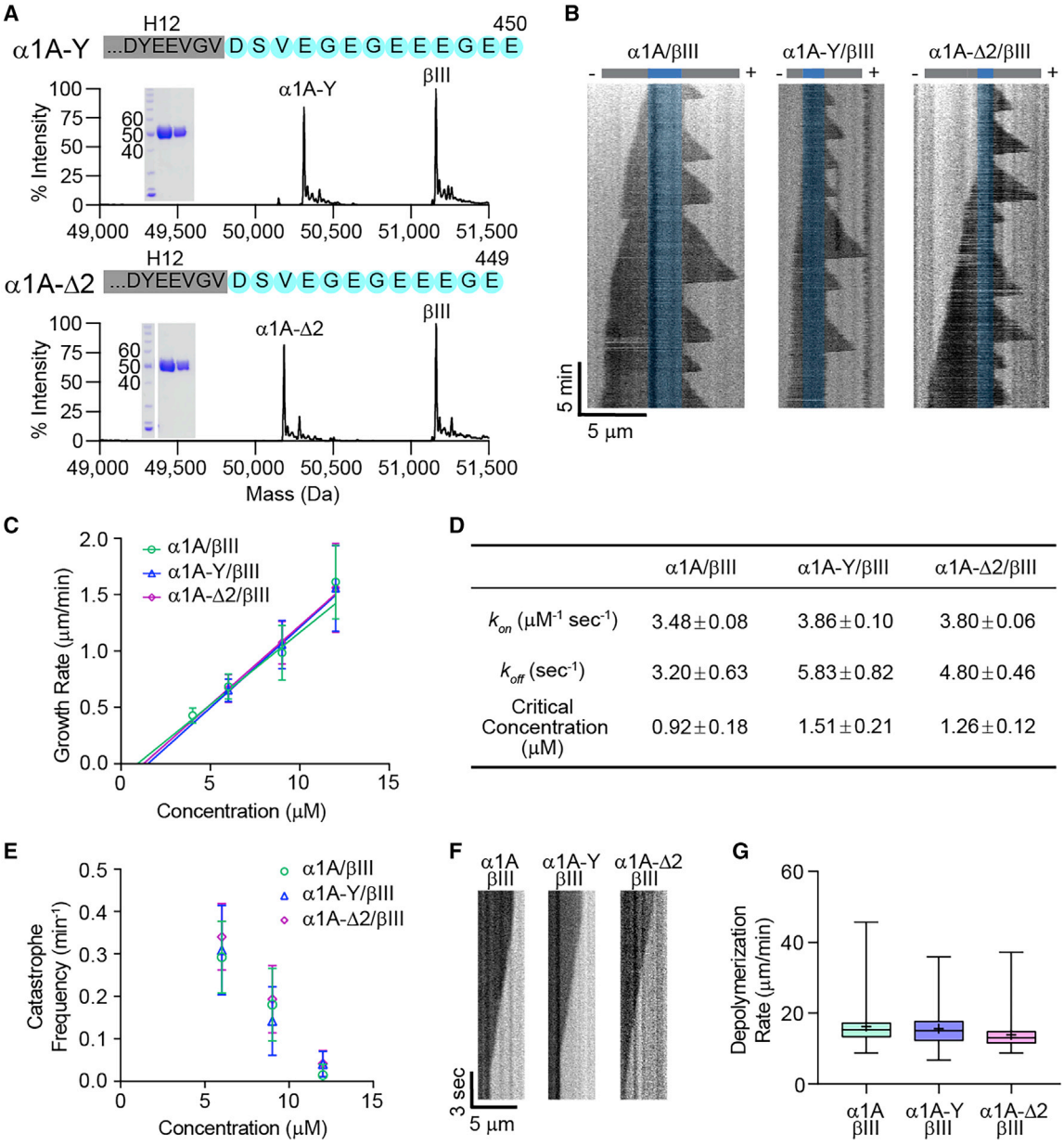

Figure 3. Tyrosinated, detyrosinated, and Δ2 microtubules have similar dynamic parameters

(A) Mass spectra and SDS-polyacrylamide gel (inset: 5 and 2 μgs of tubulin) of recombinant human α1A-Y/βIII (top) and α1A-Δ2/βIII (bottom) tubulin purified to > 99% homogeneity.

(B) Representative kymographs showing microtubule growth at 6 μM for α1A/βIII (left), α1A-Y/βIII (middle), and α1A-Δ2/βIII (right) microtubules. GMPCPP-stabilized seeds are pseudo-colored in blue.

(C) Plus-end growth rates as a function of tubulin concentration for α1A/βIII, α1A-Y/βIII, and α1A-Δ2/βIII microtubules. Error bars represent SD (n = 181, 256, 608, and 82 growth phases for α1A/βIII at 4, 6, 9, and 12 μM, respectively; n = 357, 638, 63 growth phases for α1A-Y/βIII at 6, 9, 12 μM, respectively; n = 1,139, 729, and 67 growth phases for α1A-Δ2/βIII at 6, 9, and 12 μM, respectively).

(D) Tubulin apparent on and off rates at the plus end and critical concentration determined by fitting a linear regression of the mean growth rates versus tubulin concentration shown in (C); p = 0.003 for α1A /βIII versus either α1A-Y/βIII or α1A-Δ2/βIII on-rates; p = 0.85 for α1A-Y/βIII versus α1A-Δ2/βIII on-rates. Differences in intercepts (off rate and nucleation concentration) are not statistically significant. Statistical analysis performed using a Tukey range test.

(E) Microtubule plus-end catastrophe frequencies as a function of tubulin concentration. Error bars represent SD; n = 29, 86, and 59 microtubules for α1A/βIII at 6, 9, and 12 μM, respectively; n = 37, 116, and 21 microtubules for α1A-Y/βIII at 6, 9, and 12 μM, respectively; n = 96, 97, and 22 microtubules for α1A-Δ2/βIII at 6, 9, and 12 μM, respectively.

(F) Representative kymographs showing depolymerization at 6 μM for α1A/βIII (left), α1A-Y/βIII (middle), and α1A-Δ2/βIII (right) microtubules.

(G) Box-whisker plot (whiskers indicate minimum and maximum) of depolymerization rates; n = 26, 50, and 48 growth phases for α1A/βIII, α1A-Y/βIII, and α1A-Δ2/βIII tubulin, respectively.

microtubules in cells is modulated by a large array of factors. Most notable among them are what are known as ''tip-tracking'' factors because they preferentially associate with the growing end of the microtubule (reviewed in Akhmanova and Steinmetz [2008]). The end-binding (EB) family of proteins are the master regulators at the growing microtubule end where they recruit an entire network of proteins that synergize to regulate microtubule dynamics (reviewed in Akhmanova and Steinmetz [2010a]). Among them, CLIP-170 is expressed in mammals, invertebrates, and yeast (Akhmanova et al., 2005; reviewed in Gouveia and Akhmanova [2010]), and its association with microtubules is enhanced by tubulin tyrosination (Bieling et al., 2008). Biochemical and structural studies showed that this specific recognition is mediated by the N-terminal cytoskeleton-associated protein glycine-rich (CAP-Gly) domains of CLIP-170 that recognize the terminal tyrosine in the -EEY motif present both in the C-terminal tail of α-tubulin and EB1 (Bjelić et al., 2012; Bieling et al., 2008; Mishima et al., 2007; Weisbrich et al., 2007). The association of CLIP-170 with EB1 is stronger than that with the tyrosinated α-tubulin tail (Chen et al., 2019) and CLIP-170 requires EB1 for tip-tracking (Dixit et al., 2009; Bieling et al., 2008), while detyrosination reduces CLIP-170 end tracking activity both *in vitro* (Bieling et al., 2008) and *in vivo* (Peris et al., 2006). Thus, differential tyrosination of the microtubule lattice can potentially function as a quantitative tuner of CLIP-170 recruitment to the microtubule tip and microtubule dynamics.

We used our recombinant tubulin to reconstitute a minimal tip-tracking complex with EB1 and CLIP-170 (Figure 4). We used a CLIP-170 construct, H2, which contains the two N-terminal CAP-Gly domains and part of the coiled-coil domain needed for dimerization. This construct localizes to the growing plus end both *in vitro* and in cells (Bieling et al., 2008; Perez et al., 1999; Scheel et al., 1999). We titrated α1A/βIII with α1A-Y/βIII to generate microtubules with different percentages of tyrosination (0%, 25%, 50%, 75%, and 100%). We then reconstituted GFP-H2 tip-tracking on the differentially tyrosinated microtubules (Figure 4A) and characterized the comet profiles (Figure 4B). The fluorescence intensity of GFP-H2 comets increases with tyrosination and is highest on the 100% tyrosinated microtubules (Figures 4B and 4C). This difference is due exclusively to the selective recognition of the tyrosinated tubulin by CLIP-170 as EB1 comets exhibit no distinguishable differences between α1A/βIII with α1A-Y/βIII microtubules (Figures S5A–S5C). This is consistent with previous observations which showed that treatment of brain tubulin with carboxypeptidase A, which removes residues from the C terminus of a protein, does not affect EB1 microtubule association but affects the recruitment of CLIP-170 to microtubule ends (Bieling et al., 2008). Moreover, growth-rate-matched porcine brain microtubules that are ~ 25%–50% detyrosinated (Paturle et al., 1989) show similar GFP-H2 comet profiles to those with the 50/50 tyrosinated/detyrosinated recombinant tubulin mixture, while the GFP-H2 comet intensity on growth-rate-matched tyrosinated tubulin purified from tsA201 cells (Vemu et al., 2017) is similar to that of 100% tyrosinated α1A/βIII recombinant tubulin (Figures 4B and 4C). These results indicate that tyrosination is the dominant factor recruiting CLIP-170 to microtubules of diverse tubulin isotype composition and that it quantitatively tunes the density of CLIP-170 at the growing microtubule ends.

However, does this tyrosination-dependent increase in CLIP-170 recruitment to the microtubule tip change microtubule dynamics? Quantitation of dynamic parameters on tyrosinated and detyrosinated microtubules reveals that addition of both EB1 and H2 increases the polymerization speed of tyrosinated α1A/βIII microtubules by ~50% compared with detyrosinated α1A-Y/βIII (Figures 4D and 4E). Neither EB1 nor H2 increase growth speeds individually (Figure 4E), indicating that the two factors synergize at the microtubule tip in a tyrosination-dependent manner to selectively increase the polymerization speed of tyrosinated microtubules. This effect is proportional, since having a 50/50 tyrosinated/detyrosinated tubulin mixture results in an intermediate effect on microtubule growth. The effect on growth rates depends on the amount of CLIP-170 recruited at the tip and is more modest at lower H2 concentrations (300 versus 75 nM H2; Figure S5D). Surprisingly, the two factors also synergize to increase the catastrophe frequency of tyrosinated microtubules by ~3.7-fold (Figure 4F). Again, the effect is proportional to the tyrosination levels as microtubules containing 50% tyrosinated tubulin show an intermediate effect on catastrophe rates. Neither EB1 nor H2 increase catastrophe rates individually under these conditions. The rescue frequencies of α1A/βIII and α1A-Y/βIII microtubules showed no statistically distinguishable differences when EB1 and CLIP-170 are present together (Figure 4G). However, in the absence of EB1, CLIP-170 increases selectively the rescue frequency of tyrosinated microtubules and not detyrosinated ones (Figures 4G and S6A) by binding with higher affinity along the tyrosinated microtubule lattice (Figure S6B). Taken together, our *in vitro* experiments demonstrate that tyrosination quantitatively tunes CLIP-170 recruitment to the microtubule end and that this tyrosination-dependent recruitment increases microtubule dynamicity proportionately.

DISCUSSION

In this study, we used the power of recombinant well-defined tubulin variants to interrogate the effects of the α-tubulin tail and its three abundant posttranslational modifications on microtubule dynamics. We find that the intrinsically disordered α-tubulin tail is a potent inhibitor of microtubule growth and catastrophe by regulating both the apparent on rate and off rates of tubulin at the growing microtubule end (Figure 1D). We speculate that the marked effect of the α-tail on the apparent off rate at the growing plus end is due to the fact that at the higher rates of tubulin addition of the α-tailless construct, microtubule growth is dominated by the addition of new GTP-tubulin to the GTP-cap, while in the wild-type tubulin, the rate of addition is closer matched to that of GTP hydrolysis and the tips have a mixture of GDP and GTP-tubulins, resulting in a higher apparent tubulin off rate at the growing tip. Consistent with the effect on growth, our molecular dynamics simulations reveal that the α-tubulin tail interacts with the α-tubulin body and occludes the longitudinal polymerization interface (Figure 2B). Recent NMR studies of *Tetrahymena thermophila* tubulin demonstrated that α-tubulin tail peptides have different conformations in isolation versus in the context of the αβ-tubulin dimer (Wall et al., 2016), suggesting transient interactions between the tail and the folded tubulin body that could modulate tubulin polymerization; however, the

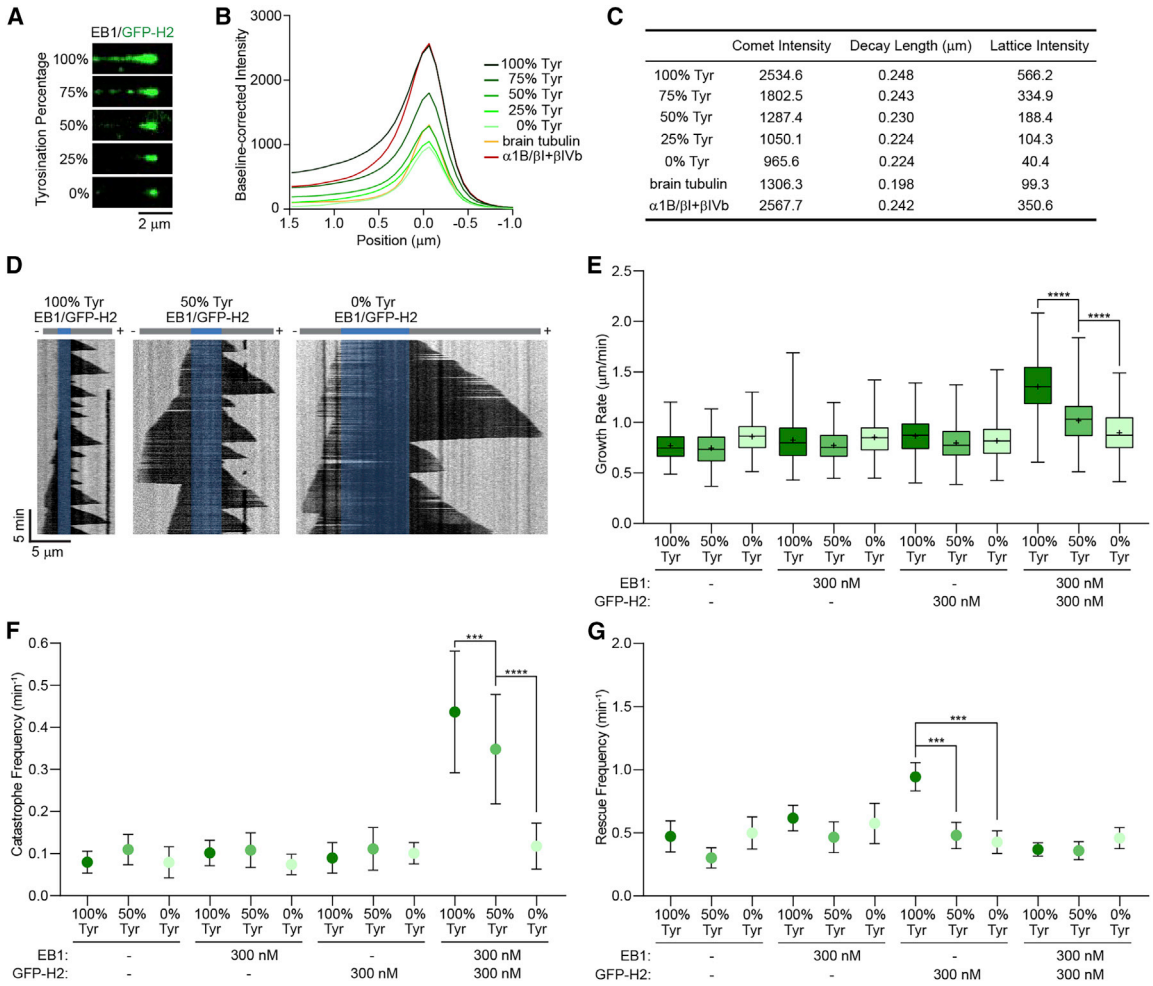

Figure 4. CLIP-170 and EB1 synergize to selectively increase the growth and catastrophe rates of tyrosinated microtubules

(A) TIRF microscopy images of GFP-H2 (75 nM, green) on recombinant microtubules with different percentages of tyrosination in the presence of 300 nM unlabeled EB1. Recombinant α1A/βIII and α1A-Y/βIII were mixed proportionally to generate a gradient of tyrosination with a total tubulin concentration of 15 μM.

(B) Averaged fluorescence intensity profiles of GFP-H2 comets on microtubules with different tyrosination content (15 μM recombinant tubulin), growth rate-matched heterogeneous brain microtubules (10 μM), and growth rate-matched α1B/βI+βIV microtubules purified from tsA201 cells (12 μM) in the presence of 300 nM unlabeled EB1.

(C) Comet profile parameters. Comet profiles were fitted using Gaussian (−1.5 to 0 μm) and single exponential functions (0 to 1.5 μm; STAR Methods); n = 1,305, 1,676, 1,890, 1,163, and 442 for recombinant tubulin with 100%, 75%, 50%, 25%, and 0% tyrosination, respectively; n = 2,500 and 1,618 for brain and α1B/βI+βIV tubulin, respectively.

(D) Representative kymographs of tyrosinated (100% Tyr; left), 50/50 tyrosinated/detyrosinated (50% Tyr; middle), and detyrosinated (0% Tyr; right) microtubules (6 μM recombinant tubulin) in the presence of 300 nM EB1 and 300 nM GFP-H2. GMPCPP-stabilized seeds are pseudo-colored in blue.

(E–G) Plus-end growth rates (E), catastrophe frequencies (F), and rescue frequencies (G) of 6 μM α1A/βIII and α1A-Y/βIII microtubules with or without 300 nM EB1 and 300 nM GFP-H2.

(E) Box-whisker plot (whiskers represent minimum and maximum) of growth rates; n = 86, 202, and 105 growth phases for 100%, 50%, 0% tyrosinated microtubules, respectively; n = 223, 247, and 80 growth phases for 100%, 50%, 0% tyrosinated microtubules with EB1, respectively; n = 223, 246, and 204 growth phases for 100%, 50%, and 0% tyrosinated microtubules with GFP-H2, respectively; n = 934, 587, and 106 growth phases for 100%, 50%, and 0% tyrosinated microtubules with EB1 and GFP-H2, respectively; **** denotes $p < 0.0001$ as determined by an unpaired t test.

(F) Catastrophe frequencies; n = 18, 33, and 22 microtubules for 100%, 50%, and 0% tyrosinated microtubules, respectively; n = 43, 39, and 17 microtubules for 100%, 50%, and 0% tyrosinated microtubules with EB1, respectively; n = 41, 43, and 36 microtubules for 100%, 50%, 0% tyrosinated microtubules with GFP-H2, respectively; n = 63, 48, and 21 microtubules for 100%, 50%, and 0% tyrosinated microtubules with EB1 and GFP-H2, respectively. Error bars indicate SD.

(G) Rescue frequencies; n values as in (F). Error bars represent SEM. **** denotes $p < 0.0001$ as determined by a Mann-Whitney test. See also Figures S5 and S6.

identity of the tubulin surfaces involved in these interactions was not assigned, nor the effects of the α-tubulin tail loss on microtubule dynamics characterized. The transient occlusion of the longitudinal polymerization interface by the α-tail is facilitated through charge-charge interactions by the large glutamate density in the α-tubulin tail. A positive effect on microtubule growth speed was recently reported after removal of the β-tubulin C-terminal tail using controlled proteolysis (Fees and Moore, 2018). However, in contrast to the α-tail, removal of the β-tail leads to an increase and not a decrease in catastrophe rates (Fees and

Moore, 2018). Thus, the two tubulin tails have evolved to have complex, distinct effects on microtubule dynamics. Since their evolution is not as tightly constrained as that of the folded polymerization interfaces, they likely evolved to provide tunable properties to the microtubule polymer.

The inhibitory role of the α-tubulin tail has interesting parallels to that recently described for a bacterial tubulin homolog from *Bacillus subtilis*, FtsZ that also uses its intrinsically disordered C-terminal tail to attenuate its incorporation into filaments (Cohan et al., 2020). More generally, intrinsically disordered regions are frequently employed in proteins to tune the equilibrium between active and inactive states (Trudeau et al., 2013). In the case of tubulin, it is important to note that the vast majority of microtubule effectors interact with the tubulin tails (Tan et al., 2019; Yadav et al., 2014; Knipling and Wolff, 2006; Westermann et al., 2005; Skiniotis et al., 2004; Wang and Sheetz, 2000; Marya et al., 1994; Serrano et al., 1985, 1984a; reviewed in Roll-Mecak [2015]), and some of them are completely dependent on the tails for high-affinity microtubule binding (Zehr et al., 2020; Roll-Mecak and Vale, 2005). Early studies demonstrated that removal of both α- and β-tubulin tails by subtilisin lowers tubulin critical concentration to that found in the presence of microtubule-associated proteins (MAPs) (Sackett et al., 1985; Serrano et al., 1984b). Thus, the occlusion of the longitudinal polymerization interface by the α-tubulin tail raises the interesting possibility that MAPs increase the tubulin on rate by sequestering and changing the dynamics of the α-tubulin tail.

In contrast to the marked effect of the α-tail on microtubule dynamics, we find that microtubules composed of detyrosinated and Δ2-tubulin have similar dynamics to tyrosinated microtubules (Figure 3D), even though these two modifications correlate strongly with increased microtubule stability in cells and are used widely as reporters for microtubule stability. However, we show that tyrosination quantitatively recruits CLIP-170 to the plus ends and facilitates a synergy between CLIP-170 and EB1 to increase growth and catastrophe rates (Figure 4), providing proof in a reconstituted system that a microtubule posttranslational modification can selectively regulate microtubule dynamic parameters through the specific recruitment of effectors. In contrast, a modification on the tubulin body also frequently used as a marker for microtubule stability in cells, Lys40 acetylation, has a direct effect on microtubule properties by protecting them from breakage (Portran et al., 2017; Xu et al., 2017).

The synergy between EB1 and CLIP-170 in promoting catastrophe on tyrosinated microtubules is surprising because CLIP-170 is largely thought of as a catastrophe suppressing factor (Martín-García and Mulvihill, 2009; Brunner and Nurse, 2000), and previous work has also shown that CLIP-170 can synergize with EB1 to elicit a modest decrease in catastrophe rates on brain microtubules (Lopus et al., 2012). EB1 on the other hand has been shown to increase catastrophe rates (Zanic et al., 2013; Vitre et al., 2008; Bieling et al., 2007), presumably by accelerating a conformational transition at the plus end of the microtubule (Zhang et al., 2018, 2015). While EB1 alters the interaction of CLIP-170 with the microtubule by recruiting it to the tip, shown in this work and many others (Dixit et al., 2009; Bieling et al., 2008; Peris et al., 2006), our data also support the model where CLIP-170 itself alters the association of EB1 at the plus end and thus possibly accelerates the kinetics of the structural transitions that lead to catastrophe. Such an interaction between EB1 and CLIP-170 is in line with previous work showing that CLIP-170 can recruit to the microtubule a truncated EB1 construct that lacks microtubule binding (Gupta et al., 2010). When not recruited to the tip by EB1, CLIP-170 promotes rescues preferentially of tyrosinated microtubules (Figure 4G), consistent with previous studies identifying it as a rescue factor (Henrie et al., 2020; Arnal et al., 2004; Komarova et al., 2002). Previous work has shown that MCAK13 selectively depolymerizes tyrosinated microtubules and this was also proposed to increase their dynamicity (Peris et al., 2009). Thus, tyrosination can act through a combination of effectors to increase microtubule turnover in cells.

We note that the α-tubulin tail -EEY motif recognized by CLIP-170 (Bjelić et al., 2012; Mishima et al., 2007; Weisbrich et al., 2007) is invariant in six of the eight α-tubulin isotypes except for α4A, and α8, (Figure S2A). α4A, which lacks the C-terminal tyrosine, is upregulated in megakaryocytes as they differentiate into platelets and is responsible for the high proportion of detyrosinated tubulin found in these cells (Strassel et al., 2019). Its loss leads to hypertyrosination and defects in establishing the stable bundle of microtubules, known as the marginal band, that is essential for differentiation into platelets (Strassel et al., 2019). We speculate that the failure to transition the cytoskeleton to this stable microtubule structure could be in part due to the increased dynamicity of the microtubules, which are now hypertyrosinated compared with wild type. Tubulin α8, which has a unique C-terminal -EEF motif, plays a critical role in cortical progenitor differentiation by not being subject to detyrosination and the subsequent terminal processing into Δ2-tubulin (Ramos et al., 2020). Since an α-tubulin tail with a terminal phenylalanine is also recognized by the CAP-Gly domain of CLIP-170 (Mishima et al., 2007; Honnappa et al., 2006), we propose that expression of α8 generates a permanent subpopulation of microtubules with increased turnover because of their persistent recruitment of CLIP-170 and possibly other factors. Thus, in addition to the dynamic tyrosination/detyrosination cycle, variations in the genetically encoded terminal residue of the α-tubulin tail itself can be used to regulate microtubule dynamics through the differential interaction with plus-end effectors.

Our experiments underscore the importance of the microtubule substrate itself in mediating the effects of microtubule regulators on microtubule dynamics and demonstrate how detyrosination or the Δ2 modification of transiently stabilized microtubules can give rise to persistent subpopulations of microtubules in cells that are less dynamic. A newly born microtubule is tyrosinated because tubulin is synthesized with a terminal tyrosine and the tubulin tyrosine ligase acts preferentially on the soluble tubulin dimer (Szyk et al., 2011; Wehland and Weber, 1987; Raybin and Flavin, 1975). The detyrosinating enzymes act preferentially on the microtubule polymer (Li et al., 2020; Wang et al., 2019; Aillaud et al., 2017; Nieuwenhuis et al., 2017; Gundersen et al., 1987; Kumar and Flavin, 1981). Thus, a transient stabilization of a microtubule can result in progressive detyrosination, which leads, as we demonstrate, to the gradual concomitant loss of tip factors that then decrease its dynamicity, thus further stabilizing the microtubule through positive feedback. The detyrosinated tubulin can further be converted to Δ2-tubulin, a modification that is irreversible and not reset through tyrosination upon depolymerization, thus permanently committing this tubulin subpopulation to slower growth and

turnover. Our work shows how the tubulin code can constitute the chemical memory of the initial stabilization, allowing it to affect cytoskeleton fate in the future.

Limitations of the study

We note that while our simulations reveal that the α-tubulin tail interacts transiently with the longitudinal polymerization interface, we could not explicitly model tubulin incorporation into the microtubule lattice or protofilaments at the microtubule tip. Thus, our conclusion that the observed marked increase in microtubule growth rates is due to this transient interaction with the polymerization interface, is a plausible extrapolation. The α1A tail is highly conserved in mammals but shows more sequence divergence in lower vertebrates, invertebrates, algae, and plants, both in length and in the number of negatively charged residues (Figure S2B). We predict that loss of the α-tail will potentiate microtubule growth, regardless of α-tubulin species or isotype; however, future biochemical and molecular dynamics studies will be needed to establish whether loss of the α-tail leads to similar magnitude effects on microtubule growth rates in these cases as we observe here for the human isotype. More recent work also revealed the existence of Δ3-tubulin in neuronal tissue, which misses the last three residues (EEY) of the α-tubulin tail (Aillaud et al., 2016). It is unclear whether the loss of one more glutamate in the Δ3-tubulin will have a pronounced effect on growth rates compared with Δ2-tubulin due to a reduced interaction of the tail with the polymerization interface. Our simulations predict that the effect would be modest because of the cumulative small contributions that each tail residue has out of the total of 12, but this will only be established with certainty through future experimental work.

STAR★METHODS

Detailed methods are provided in the online version of this paper and include the following:

- KEY RESOURCES TABLE
- RESOURCE AVAILABILITY
  - Lead contact
  - Material availability
  - Data and code availability
- EXPERIMENTAL MODEL AND SUBJECT DETAILS
- METHOD DETAILS
  - Purification of recombinant tubulin isotypes
  - Purification of GFP-H2 and EB1
  - *In vitro* microtubule dynamics assays
  - EB1 and CLIP170 *in vitro* tip-tracking
  - MD simulations
  - Metadynamics simulations of α-tail interactions
- QUANTIFICATION AND STATISTICAL ANALYSIS
  - Microtubule dynamics analysis
  - EB1 and CLIP-170 plus-end tracking analysis
  - Analysis of α-tubulin tail dynamics in MD simulations

SUPPLEMENTAL INFORMATION

Supplemental Information can be found online at https://doi.org/10.1016/j.devcel.2021.05.005.

ACKNOWLEDGMENTS

We thank Jeff Spector (National Institute of Neurological Disorders and Stroke) for help with comet analysis, Annapurna Vemu (National Institute of Neurological Disorders and Stroke) for advice on microtubule dynamics assays and initial efforts on the project, D-Y. Lee from the Biophysics Core (National Heart, Lung and Blood Institute) for mass spectrometry access and advice, and Thomas Surrey (Center for Genomic Regulation) for the GFP-H2 plasmid. A.R.-M. is supported by the intramural programs of the National Institute of Neurological Disorders and Stroke (NINDS) and the National Heart, Lung and Blood Institute (NHLBI). MD simulations were done with support from the Interdisciplinary Scientific and Educational School of Moscow University Photonic and Quantum Technologies. Digital Medicine, Russian Foundation for Basic Research (research project #20-34-70159) and RF President's grant MK-1869.2020.4 to N.G., using the equipment of the shared research facilities of the high-performance computational resources at Lomonosov Moscow State University.

AUTHOR CONTRIBUTIONS

J.C. performed and analyzed all dynamics assays and purified proteins. A.S. cloned all constructs and purified proteins. E.K., V.A.F., I.K., and N.G. performed MD simulations and analyses. A.R.-M. initiated, conceptualized, and supervised project. A.R.-M., J.C., and N.G. interpreted data and wrote the manuscript. All authors read, edited, and approved the manuscript.

DECLARATION OF INTERESTS

The authors declare no competing interests.

Received: March 1, 2021
Revised: April 26, 2021
Accepted: May 5, 2021
Published: May 21, 2021

REFERENCES

Aillaud, C., Bosc, C., Peris, L., Bosson, A., Heemeryck, P., Van Dijk, J., Le Friec, J., Boulan, B., Vossier, F., Sanman, L.E., et al. (2017). Vasohibins/SVBP are tubulin carboxypeptidaseS (TCPs) that regulate neuron differentiation. Science *358*, 1448–1453.

Aillaud, C., Bosc, C., Saoudi, Y., Denarier, E., Peris, L., Sago, L., Taulet, N., Cieren, A., Tort, O., Magiera, M.M., et al. (2016). Evidence for new C-terminally truncated variants of alpha- and beta-tubulins. Mol. Biol. Cell *27*, 640–653.

Akera, T., Chmátal, L., Trimm, E., Yang, K., Aonbangkhen, C., Chenoweth, D.M., Janke, C., Schultz, R.M., and Lampson, M.A. (2017). Spindle asymmetry drives non-Mendelian chromosome segregation. Science *358*, 668–672.

Akhmanova, A., Mausset-Bonnefont, A.L., van Cappellen, W., Keijzer, N., Hoogenraad, C.C., Stepanova, T., Drabek, K., van der Wees, J., Mommaas, M., Onderwater, J., et al. (2005). The microtubule plus-end-tracking protein CLIP-170 associates with the spermatid manchette and is essential for spermatogenesis. Genes Dev *19*, 2501–2515.

Akhmanova, A., and Steinmetz, M.O. (2008). Tracking the ends: a dynamic protein network controls the fate of microtubule tips. Nat. Rev. Mol. Cell Biol. *9*, 309–322.

Akhmanova, A., and Steinmetz, M.O. (2010a). Microtubule +TIPs at a glance. J. Cell Sci. *123*, 3415–3419.

Alfaro-Aco, R., and Petry, S. (2015). Building the microtubule cytoskeleton piece by piece. J. Biol. Chem. *290*, 17154–17162.

Alushin, G.M., Lander, G.C., Kellogg, E.H., Zhang, R., Baker, D., and Nogales, E. (2014). High-resolution microtubule structures reveal the structural transitions in αβ-tubulin upon GTP hydrolysis. Cell *157*, 1117–1129.

Alushin, G.M., Ramey, V.H., Pasqualato, S., Ball, D.A., Grigorieff, N., Musacchio, A., and Nogales, E. (2010). The Ndc80 kinetochore complex forms oligomeric arrays along microtubules. Nature *467*, 805–810.

Argaraña, C.E., Barra, H.S., and Caputto, R. (1978). Release of [14C]tyrosine from tubulinyl-[14C]tyrosine by brain extract. Separation of a carboxypeptidase from tubulin-tyrosine ligase. Mol. Cell. Biochem. *19*, 17–21.

Arnal, I., Heichette, C., Diamantopoulos, G.S., and Chrétien, D. (2004). CLIP-170/tubulin-curved oligomers coassemble at microtubule ends and promote rescues. Curr. Biol. *14*, 2086–2095.

Barisic, M., Silva e Sousa, R., Tripathy, S.K., Magiera, M.M., Zaytsev, A.V., Pereira, A.L., Janke, C., Grishchuk, E.L., and Maiato, H. (2015). Mitosis. Microtubule detyrosination guides chromosomes during mitosis. Science *348*, 799–803.

Barra, H.S., Rodriguez, J.A., Arce, C.A., and Caputto, R. (1973). A soluble preparation from rat brain that incorporates into its own proteins (14 C)arginine by a ribonuclease-sensitive system and (14 C)tyrosine by a ribonuclease-insensitive system. J. Neurochem. *20*, 97–108.

Bhattacharyya, B., Sackett, D.L., and Wolff, J. (1985). Tubulin, hybrid dimers, and tubulin S. Stepwise charge reduction and polymerization. J. Biol. Chem. *260*, 10208–10216.

Bieling, P., Kandels-Lewis, S., Telley, I.A., van Dijk, J., Janke, C., and Surrey, T. (2008). CLIP-170 tracks growing microtubule ends by dynamically recognizing composite EB1/tubulin-binding sites. J. Cell Biol. *183*, 1223–1233.

Bieling, P., Laan, L., Schek, H., Munteanu, E.L., Sandblad, L., Dogterom, M., Brunner, D., and Surrey, T. (2007). Reconstitution of a microtubule plus-end tracking system in vitro. Nature *450*, 1100–1105.

Bjelić, S., De Groot, C.O., Schärer, M.A., Jaussi, R., Bargsten, K., Salzmann, M., Frey, D., Capitani, G., Kammerer, R.A., and Steinmetz, M.O. (2012). Interaction of mammalian end binding proteins with CAP-Gly domains of CLIP-170 and p150(glued). J. Struct. Biol. *177*, 160–167.

Brunner, D., and Nurse, P. (2000). CLIP170-like tip1p spatially organizes microtubular dynamics in fission yeast. Cell *102*, 695–704.

Carlier, M.F. (1982). Guanosine-5'-triphosphate hydrolysis and tubulin polymerization. Review article. Mol. Cell. Biochem. *47*, 97–113.

Carlier, M.F., and Pantaloni, D. (1981). Kinetic analysis of guanosine 5′-triphosphate hydrolysis associated with tubulin polymerization. Biochemistry *20*, 1918–1924.

Chang, W., Webster, D.R., Salam, A.A., Gruber, D., Prasad, A., Eiserich, J.P., and Bulinski, J.C. (2002). Alteration of the C-terminal amino acid of tubulin specifically inhibits myogenic differentiation. J. Biol. Chem. *277*, 30690–30698.

Chen, Y., Wang, P., and Slep, K.C. (2019). Mapping multivalency in the CLIP-170-EB1 microtubule plus-end complex. J. Biol. Chem. *294*, 918–931.

Cohan, M.C., Eddelbuettel, A.M.P., Levin, P.A., and Pappu, R.V. (2020). Dissecting the functional contributions of the intrinsically disordered C-terminal tail of Bacillus subtilis FtsZ. J. Mol. Biol. *432*, 3205–3221.

Dixit, R., Barnett, B., Lazarus, J.E., Tokito, M., Goldman, Y.E., and Holzbaur, E.L. (2009). Microtubule plus-end tracking by CLIP-170 requires EB1. Proc. Natl. Acad. Sci. US.A *106*, 492–497.

Duellberg, C., Cade, N.I., Holmes, D., and Surrey, T. (2016). The size of the EB cap determines instantaneous microtubule stability. eLife *5*, e13470.

Erck, C., Peris, L., Andrieux, A., Meissirel, C., Gruber, A.D., Vernet, M., Schweitzer, A., Saoudi, Y., Pointu, H., Bosc, C., et al. (2005). A vital role of tubulin-tyrosine-ligase for neuronal organization. Proc. Natl. Acad. Sci. USA *102*, 7853–7858.

Fedorov, V.A., Kholina, E.G., Kovalenko, I.B., and Gudimchuk, N. (2018). Performance analysis of different computational architectures: molecular dynamics in application to protein assemblies, illustrated by microtubule and electron transfer proteins. Supercomput. Front. Innov. *5*, 111–114.

Fedorov, V.A., Orekhov, P.S., Kholina, E.G., Zhmurov, A.A., Ataullakhanov, F.I., Kovalenko, I.B., and Gudimchuk, N.B. (2019). Mechanical properties of tubulin intra- and inter-dimer interfaces and their implications for microtubule dynamic instability. PLoS Comput. Biol. *15*, e1007327.

Feenstra, K.A., Hess, B., and Berendsen, H.J.C. (1999). Improving efficiency of large time-scale molecular dynamics simulations of hydrogen-rich systems. J. Comput. Chem. *20*, 786–798.

Fees, C.P., and Moore, J.K. (2018). Regulation of microtubule dynamic instability by the carboxy-terminal tail of beta-tubulin. Life Sci. Alliance *1*, e201800054.

Flavin, M., and Murofushi, H. (1984). Tyrosine incorporation in tubulin. Methods Enzymol *106*, 223–237.

Garnham, C.P., Vemu, A., Wilson-Kubalek, E.M., Yu, I., Szyk, A., Lander, G.C., Milligan, R.A., and Roll-Mecak, A. (2015). Multivalent microtubule recognition by tubulin tyrosine ligase-like family glutamylases. Cell *161*, 1112–1123.

Gell, C., Bormuth, V., Brouhard, G.J., Cohen, D.N., Diez, S., Friel, C.T., Helenius, J., Nitzsche, B., Petzold, H., Ribbe, J., et al. (2010). Microtubule dynamics reconstituted in vitro and imaged by single-molecule fluorescence microscopy. Methods Cell Biol *95*, 221–245.

Gouveia, S.M., and Akhmanova, A. (2010). Cell and molecular biology of microtubule plus end tracking proteins: end binding proteins and their partners. Int. Rev. Cell Mol. Biol. *285*, 1–74.

Gundersen, G.G., and Bulinski, J.C. (1986a). Distribution of tyrosinated and nontyrosinated alpha-tubulin during mitosis. J. Cell Biol. *102*, 1118–1126.

Gundersen, G.G., and Bulinski, J.C. (1986b). Microtubule arrays in differentiated cells contain elevated levels of a post-translationally modified form of tubulin. Eur. J. Cell Biol. *42*, 288–294.

Gundersen, G.G., and Bulinski, J.C. (1988). Selective stabilization of microtubules oriented toward the direction of cell migration. Proc. Natl. Acad. Sci. USA *85*, 5946–5950.

Gundersen, G.G., Khawaja, S., and Bulinski, J.C. (1987). Postpolymerization detyrosination of alpha-tubulin: a mechanism for subcellular differentiation of microtubules. J. Cell Biol. *105*, 251–264.

Gundersen, G.G., Khawaja, S., and Bulinski, J.C. (1989). Generation of a stable, posttranslationally modified microtubule array is an early event in myogenic differentiation. J. Cell Biol. *109*, 2275–2288.

Gupta, K.K., Joyce, M.V., Slabbekoorn, A.R., Zhu, Z.C., Paulson, B.A., Boggess, B., and Goodson, H.V. (2010). Probing interactions between CLIP-170, EB1, and microtubules. J. Mol. Biol. *395*, 1049–1062.

Henrie, H., Bakhos-Douaihy, D., Cantaloube, I., Pilon, A., Talantikite, M., Stoppin-Mellet, V., Baillet, A., Poüs, C., and Benoit, B. (2020). Stress-induced phosphorylation of CLIP-170 by JNK promotes microtubule rescue. J. Cell Biol. *219*, e201909093.

Honnappa, S., Okhrimenko, O., Jaussi, R., Jawhari, H., Jelesarov, I., Winkler, F.K., and Steinmetz, M.O. (2006). Key interaction modes of dynamic +TIP networks. Mol. Cell *23*, 663–671.

Horio, T.H., and Hotani, H. (1986). Visualization of the dynamic instability of individual microtubules by dark-field microscopy. Nature *321*, 605–607.

Infante, A.S., Stein, M.S., Zhai, Y., Borisy, G.G., and Gundersen, G.G. (2000). Detyrosinated (Glu) microtubules are stabilized by an ATP-sensitive plus-end cap. J. Cell Sci. *113*, 3907–3919.

Iwata-Otsubo, A., Dawicki-McKenna, J.M., Akera, T., Falk, S.J., Chmátal, L., Yang, K., Sullivan, B.A., Schultz, R.M., Lampson, M.A., and Black, B.E. (2017). Expanded satellite repeats amplify a discrete CENP-A nucleosome assembly site on chromosomes that drive in female meiosis. Curr. Biol. *27*, 2365–2373, e8.

Janke, C., and Magiera, M.M. (2020). The tubulin code and its role in controlling microtubule properties and functions. Nat. Rev. Mol. Cell Biol. *21*, 307–326.

Khawaja, S., Gundersen, G.G., and Bulinski, J.C. (1988). Enhanced stability of microtubules enriched in detyrosinated tubulin is not a direct function of detyrosination level. J. Cell Biol. *106*, 141–149.

Khruschev, S.S., Abaturova, A.M., Diakonova, A.N., Fedorov, V.A., Ustinin, D.M., Kovalenko, I.B., Riznichenko, G.Y., and Rubin, A.B. (2015). Brownian dynamics simulations of protein-protein interactions in photosynthetic electron transport chain. Biofizika *60*, 270–292.

Kirschner, M., and Mitchison, T. (1986). Beyond self-assembly: from microtubules to morphogenesis. Cell *45*, 329–342.

Knipling, L., Hwang, J., and Wolff, J. (1999). Preparation and properties of pure tubulin S. Cell Motil. Cytoskeleton *43*, 63–71.

Knipling, L., and Wolff, J. (2006). Direct interaction of Bcl-2 proteins with tubulin. Biochem. Biophys. Res. Commun. *341*, 433–439.

Komarova, Y.A., Akhmanova, A.S., Kojima, S., Galjart, N., and Borisy, G.G. (2002). Cytoplasmic linker proteins promote microtubule rescue in vivo. J. Cell Biol. *159*, 589–599.

Kreis, T.E. (1987). Microtubules containing detyrosinated tubulin are less dynamic. EMBO J *6*, 2597–2606.

Kreitzer, G., Liao, G., and Gundersen, G.G. (1999). Detyrosination of tubulin regulates the interaction of intermediate filaments with microtubules in vivo via a kinesin-dependent mechanism. Mol. Biol. Cell *10*, 1105–1118.

Kumar, N., and Flavin, M. (1981). Preferential action of a brain detyrosinolating carboxypeptidase on polymerized tubulin. J. Biol. Chem. *256*, 7678–7686.

Li, F., Li, Y., Ye, X., Gao, H., Shi, Z., Luo, X., Rice, L.M., and Yu, H. (2020). Cryo-EM structure of VASH1-SVBP bound to microtubules. eLife *9*, e58157.

Lopus, M., Manatschal, C., Buey, R.M., Bjelić, S., Miller, H.P., Steinmetz, M.O., and Wilson, L. (2012). Cooperative stabilization of microtubule dynamics by EB1 and CLIP-170 involves displacement of stably bound P(i) at microtubule ends. Biochemistry *51*, 3021–3030.

Ludueña, R.F. (2013). A hypothesis on the origin and evolution of tubulin. Int. Rev. Cell Mol. Biol. *302*, 41–185.

MacKerell, A.D., Bashford, D., Bellott, M., Dunbrack, R.L., Evanseck, J.D., Field, M.J., Fischer, S., Gao, J., Guo, H., Ha, S., et al. (1998). All-atom empirical potential for molecular modeling and dynamics studies of proteins. J. Phys. Chem. B *102*, 3586–3616.

MacKerell, A.D., Jr., Feig, M., and Brooks, C.L., 3rd. (2004). Improved treatment of the protein backbone in empirical force fields. J. Am. Chem. Soc. *126*, 698–699.

Mahamdeh, M., Simmert, S., Luchniak, A., Schäffer, E., and Howard, J. (2018). Label-free high-speed wide-field imaging of single microtubules using interference reflection microscopy. J. Microsc. *272*, 60–66.

Marcos, S., Moreau, J., Backer, S., Job, D., Andrieux, A., and Bloch-Gallego, E. (2009). Tubulin tyrosination is required for the proper organization and pathfinding of the growth cone. PLoS One *4*, e5405.

Martín-García, R., and Mulvihill, D.P. (2009). Myosin V spatially regulates microtubule dynamics and promotes the ubiquitin-dependent degradation of the fission yeast CLIP-170 homologue. Tip1. J. Cell Sci. *122*, 3862–3872.

Marya, P.K., Syed, Z., Fraylich, P.E., and Eagles, P.A. (1994). Kinesin and tau bind to distinct sites on microtubules. J. Cell Sci. *107*, 339–344.

McGibbon, R.T., Beauchamp, K.A., Harrigan, M.P., Klein, C., Swails, J.M., Hernández, C.X., Schwantes, C.R., Wang, L.P., Lane, T.J., and Pande, V.S. (2015). MDTraj: a modern open library for the analysis of molecular dynamics trajectories. Biophys. J. *109*, 1528–1532.

McKenney, R.J., Huynh, W., Vale, R.D., and Sirajuddin, M. (2016). Tyrosination of alpha-tubulin controls the initiation of processive dynein-dynactin motility. EMBO J *35*, 1175–1185.

Minoura, I., Hachikubo, Y., Yamakita, Y., Takazaki, H., Ayukawa, R., Uchimura, S., and Muto, E. (2013). Overexpression, purification, and functional analysis of recombinant human tubulin dimer. FEBS Lett *587*, 3450–3455.

Mishima, M., Maesaki, R., Kasa, M., Watanabe, T., Fukata, M., Kaibuchi, K., and Hakoshima, T. (2007). Structural basis for tubulin recognition by cytoplasmic linker protein 170 and its autoinhibition. Proc. Natl. Acad. Sci. USA *104*, 10346–10351.

Mitchison, T., and Kirschner, M. (1984). Dynamic instability of microtubule growth. Nature *312*, 237–242.

Morozenko, A., and Stuchebrukhov, A.A. (2016). Dowser++, a new method of hydrating protein structures. Proteins *84*, 1347–1357.

Nieuwenhuis, J., Adamopoulos, A., Bleijerveld, O.B., Mazouzi, A., Stickel, E., Celie, P., Altelaar, M., Knipscheer, P., Perrakis, A., Blomen, V.A., and Brummelkamp, T.R. (2017). Vasohibins encode tubulin detyrosinating activity. Science *358*, 1453–1456.

Nirschl, J.J., Magiera, M.M., Lazarus, J.E., Janke, C., and Holzbaur, E.L. (2016). Alpha-tubulin tyrosination and CLIP-170 phosphorylation regulate the initiation of dynein-driven transport in neurons. Cell Rep *14*, 2637–2652.

Olsson, M.H., Søndergaard, C.R., Rostkowski, M., and Jensen, J.H. (2011). PROPKA3: consistent treatment of internal and surface residues in empirical pKa predictions. J. Chem. Theory Comput. *7*, 525–537.

Oosawa, F. (1970). Size distribution of protein polymers. J. Theor. Biol. *27*, 69–86.

Parrinello, M., and Rahman, A. (1981). Polymorphic transitions in single crystals: A new molecular dynamics method. J. Appl. Phys. *52*, 7182–7190.

Paturle, L., Wehland, J., Margolis, R.L., and Job, D. (1989). Complete separation of tyrosinated, detyrosinated, and nontyrosinatable brain tubulin subpopulations using affinity chromatography. Biochemistry *28*, 2698–2704.

Paturle-Lafanechère, L., Eddé, B., Denoulet, P., Van Dorsselaer, A., Mazarguil, H., Le Caer, J.P., Wehland, J., and Job, D. (1991). Characterization of a major brain tubulin variant which cannot be tyrosinated. Biochemistry *30*, 10523–10528.

Paturle-Lafanechère, L., Manier, M., Trigault, N., Pirollet, F., Mazarguil, H., and Job, D. (1994). Accumulation of delta 2-tubulin, a major tubulin variant that cannot be tyrosinated, in neuronal tissues and in stable microtubule assemblies. J. Cell Sci. *107*, 1529–1543.

Perez, F., Diamantopoulos, G.S., Stalder, R., and Kreis, T.E. (1999). CLIP-170 highlights growing microtubule ends in vivo. Cell *96*, 517–527.

Peris, L., Thery, M., Fauré, J., Saoudi, Y., Lafanechère, L., Chilton, J.K., Gordon-Weeks, P., Galjart, N., Bornens, M., Wordeman, L., et al. (2006). Tubulin tyrosination is a major factor affecting the recruitment of CAP-Gly proteins at microtubule plus ends. J. Cell Biol. *174*, 839–849.

Peris, L., Wagenbach, M., Lafanechère, L., Brocard, J., Moore, A.T., Kozielski, F., Job, D., Wordeman, L., and Andrieux, A. (2009). Motor-dependent microtubule disassembly driven by tubulin tyrosination. J. Cell Biol. *185*, 1159–1166.

Petry, S., Pugieux, C., Nédélec, F.J., and Vale, R.D. (2011). Augmin promotes meiotic spindle formation and bipolarity in Xenopus egg extracts. Proc. Natl. Acad. Sci. USA *108*, 14473–14478.

Portran, D., Schaedel, L., Xu, Z., Théry, M., and Nachury, M.V. (2017). Tubulin acetylation protects long-lived microtubules against mechanical ageing. Nat. Cell Biol. *19*, 391–398.

Ramos, S.I., Makeyev, E.V., Salierno, M., Kodama, T., Kawakami, Y., and Sahara, S. (2020). Tuba8 drives differentiation of cortical radial glia into apical intermediate progenitors by tuning modifications of tubulin C Termini. Dev. Cell *52*, 477–491.e8.

Raybin, D., and Flavin, M. (1975). An enzyme tyrosylating alpha-tubulin and its role in microtubule assembly. Biochem. Biophys. Res. Commun. *65*, 1088–1095.

Raybin, D., and Flavin, M. (1977). Enzyme which specifically adds tyrosine to the alpha chain of tubulin. Biochemistry *16*, 2189–2194.

Robert, X., and Gouet, P. (2014). Deciphering key features in protein structures with the new ENDscript server. Nucleic Acids Res *42*, W320–W324.

Robison, P., Caporizzo, M.A., Ahmadzadeh, H., Bogush, A.I., Chen, C.Y., Margulies, K.B., Shenoy, V.B., and Prosser, B.L. (2016). Detyrosinated microtubules buckle and bear load in contracting cardiomyocytes. Science *352*, aaf0659.

Robson, S.J., and Burgoyne, R.D. (1989). Differential localisation of tyrosinated, detyrosinated, and acetylated alpha-tubulins in neurites and growth cones of dorsal root ganglion neurons. Cell Motil. Cytoskeleton *12*, 273–282.

Roll-Mecak, A. (2015). Intrinsically disordered tubulin tails: complex tuners of microtubule functions? Semin. Cell Dev. Biol. *37*, 11–19.

Roll-Mecak, A. (2019). How cells exploit tubulin diversity to build functional cellular microtubule mosaics. Curr. Opin. Cell Biol. *56*, 102–108.

Roll-Mecak, A. (2020). The tubulin code in microtubule dynamics and information encoding. Dev. Cell *54*, 7–20.

Roll-Mecak, A., and Vale, R.D. (2005). The Drosophila homologue of the hereditary spastic paraplegia protein, spastin, severs and disassembles microtubules. Curr. Biol. *15*, 650–655.

Sackett, D.L., Bhattacharyya, B., and Wolff, J. (1985). Tubulin subunit carboxyl termini determine polymerization efficiency. J. Biol. Chem. *260*, 43–45.

Scheel, J., Pierre, P., Rickard, J.E., Diamantopoulos, G.S., Valetti, C., van der Goot, F.G., Häner, M., Aebi, U., and Kreis, T.E. (1999). Purification and analysis of authentic CLIP-170 and recombinant fragments. J. Biol. Chem. *274*, 25883–25891.

Schindelin, J., Arganda-Carreras, I., Frise, E., Kaynig, V., Longair, M., Pietzsch, T., Preibisch, S., Rueden, C., Saalfeld, S., Schmid, B., et al. (2012). Fiji: an open-source platform for biological-image analysis. Nat. Methods *9*, 676–682.

Schulze, E., and Kirschner, M. (1987). Dynamic and stable populations of microtubules in cells. J. Cell Biol. *104*, 277–288.

Serrano, L., Avila, J., and Maccioni, R.B. (1984a). Controlled proteolysis of tubulin by subtilisin: localization of the site for MAP2 interaction. Biochemistry *23*, 4675–4681.

Serrano, L., de la Torre, J., Maccioni, R.B., and Avila, J. (1984b). Involvement of the carboxyl-terminal domain of tubulin in the regulation of its assembly. Proc. Natl. Acad. Sci. USA *81*, 5989–5993.

Serrano, L., Montejo de Garcini, E., Hernández, M.A., and Avila, J. (1985). Localization of the tubulin binding site for Tau protein. Eur. J. Biochem. *153*, 595–600.

Serrano, L., Wandosell, F., de la Torre, J., and Avila, J. (1988). Effect of specific proteolytic cleavages on tubulin polymer formation. Biochem. J. *252*, 683–691.

Shintani, T., Ihara, M., Tani, S., Sakuraba, J., Sakuta, H., and Noda, M. (2009). APC2 plays an essential role in axonal projections through the regulation of microtubule stability. J. Neurosci. *29*, 11628–11640.

Sirajuddin, M., Rice, L.M., and Vale, R.D. (2014). Regulation of microtubule motors by tubulin isotypes and post-translational modifications. Nat. Cell Biol. *16*, 335–344.

Skiniotis, G., Cochran, J.C., Müller, J., Mandelkow, E., Gilbert, S.P., and Hoenger, A. (2004). Modulation of kinesin binding by the C-termini of tubulin. EMBO J *23*, 989–999.

Strassel, C., Magiera, M.M., Dupuis, A., Batzenschlager, M., Hovasse, A., Pleines, I., Guéguen, P., Eckly, A., Moog, S., Mallo, L., et al. (2019). An essential role for α4A-tubulin in platelet biogenesis. Life Sci. Alliance *2*, e201900309.

Szyk, A., Deaconescu, A.M., Piszczek, G., and Roll-Mecak, A. (2011). Tubulin tyrosine ligase structure reveals adaptation of an ancient fold to bind and modify tubulin. Nat. Struct. Mol. Biol. *18*, 1250–1258.

Tan, R., Lam, A.J., Tan, T., Han, J., Nowakowski, D.W., Vershinin, M., Simó, S., Ori-McKenney, K.M., and McKenney, R.J. (2019). Microtubules gate tau condensation to spatially regulate microtubule functions. Nat. Cell Biol. *21*, 1078–1085.

Ti, S.C., Alushin, G.M., and Kapoor, T.M. (2018). Human beta-tubulin Isotypes Can Regulate Microtubule protofilament Number and Stability. Dev. Cell *47*, 175–190.e5.

Tribello, G.A., Bonomi, M., Branduardi, D., Camilloni, C., and Bussi, G. (2014). PLUMED 2: New feathers for an old bird. Comput. Phys. Commun. *185*, 604–613.

Trudeau, T., Nassar, R., Cumberworth, A., Wong, E.T., Woollard, G., and Gsponer, J. (2013). Structure and intrinsic disorder in protein autoinhibition. Structure *21*, 332–341.

Vemu, A., Atherton, J., Spector, J.O., Moores, C.A., and Roll-Mecak, A. (2017). Tubulin isoform composition tunes microtubule dynamics. Mol. Biol. Cell *28*, 3564–3572.

Vemu, A., Atherton, J., Spector, J.O., Szyk, A., Moores, C.A., and Roll-Mecak, A. (2016). Structure and dynamics of single-isoform recombinant neuronal human tubulin. J. Biol. Chem. *291*, 12907–12915.

Verhey, K.J., and Gaertig, J. (2007). The tubulin code. Cell Cycle *6*, 2152–2160.

Vigers, G.P., Coue, M., and McIntosh, J.R. (1988). Fluorescent microtubules break up under illumination. J. Cell Biol. *107*, 1011–1024.

Vitre, B., Coquelle, F.M., Heichette, C., Garnier, C., Chrétien, D., and Arnal, I. (2008). EB1 regulates microtubule dynamics and tubulin sheet closure in vitro. Nat. Cell Biol. *10*, 415–421.

Walker, R.A., O'Brien, E.T., Pryer, N.K., Soboeiro, M.F., Voter, W.A., Erickson, H.P., and Salmon, E.D. (1988). Dynamic instability of individual microtubules analyzed by video light microscopy: rate constants and transition frequencies. J. Cell Biol. *107*, 1437–1448.

Wall, K.P., Pagratis, M., Armstrong, G., Balsbaugh, J.L., Verbeke, E., Pearson, C.G., and Hough, L.E. (2016). Molecular determinants of tubulin's C-terminal tail conformational ensemble. ACS Chem. Biol. *11*, 2981–2990.

Wang, N., Bosc, C., Ryul Choi, S., Boulan, B., Peris, L., Olieric, N., Bao, H., Krichen, F., Chen, L., Andrieux, A., et al. (2019). Structural basis of tubulin detyrosination by the vasohibin-SVBP enzyme complex. Nat. Struct. Mol. Biol. *26*, 571–582.

Wang, Z., and Sheetz, M.P. (2000). The C-terminus of tubulin increases cytoplasmic dynein and kinesin processivity. Biophys. J. *78*, 1955–1964.

Waterhouse, A.M., Procter, J.B., Martin, D.M., Clamp, M., and Barton, G.J. (2009). Jalview Version 2–a multiple sequence alignment editor and analysis workbench. Bioinformatics *25*, 1189–1191.

Webb, B., and Sali, A. (2014). Comparative protein structure modeling using MODELLER. Curr. Protoc. Bioinformatics *47*, 1–32.

Webster, D.R., and Borisy, G.G. (1989). Microtubules are acetylated in domains that turn over slowly. J. Cell Sci. *92*, 57–65.

Webster, D.R., Gundersen, G.G., Bulinski, J.C., and Borisy, G.G. (1987a). Assembly and turnover of detyrosinated tubulin in vivo. J. Cell Biol. *105*, 265–276.

Webster, D.R., Gundersen, G.G., Bulinski, J.C., and Borisy, G.G. (1987b). Differential turnover of tyrosinated and detyrosinated microtubules. Proc. Natl. Acad. Sci. USA *84*, 9040–9044.

Wehland, J., and Weber, K. (1987). Turnover of the carboxy-terminal tyrosine of alpha-tubulin and means of reaching elevated levels of detyrosination in living cells. J. Cell Sci. *88*, 185–203.

Weisbrich, A., Honnappa, S., Jaussi, R., Okhrimenko, O., Frey, D., Jelesarov, I., Akhmanova, A., and Steinmetz, M.O. (2007). Structure-function relationship of CAP-Gly domains. Nat. Struct. Mol. Biol. *14*, 959–967.

Weisenberg, R.C. (1972). Microtubule formation in vitro in solutions containing low calcium concentrations. Science *177*, 1104–1105.

Westermann, S., Avila-Sakar, A., Wang, H.W., Niederstrasser, H., Wong, J., Drubin, D.G., Nogales, E., and Barnes, G. (2005). Formation of a dynamic kinetochore- microtubule interface through assembly of the Dam1 ring complex. Mol. Cell *17*, 277–290.

Whipple, R.A., Matrone, M.A., Cho, E.H., Balzer, E.M., Vitolo, M.I., Yoon, J.R., Ioffe, O.B., Tuttle, K.C., Yang, J., and Martin, S.S. (2010). Epithelial-to-mesenchymal transition promotes tubulin detyrosination and microtentacles that enhance endothelial engagement. Cancer Res *70*, 8127–8137.

White, E.A., Burton, P.R., and Himes, R.H. (1987). Polymorphic assembly of subtilisin-cleaved tubulin. Cell Motil. Cytoskeleton *7*, 31–38.

Witte, H., Neukirchen, D., and Bradke, F. (2008). Microtubule stabilization specifies initial neuronal polarization. J. Cell Biol. *180*, 619–632.

Xu, P., Das, M., Reilly, J., and Davis, R.J. (2011). JNK regulates FoxO-dependent autophagy in neurons. Genes Dev *25*, 310–322.

Xu, Z., Schaedel, L., Portran, D., Aguilar, A., Gaillard, J., Marinkovich, M.P., Théry, M., and Nachury, M.V. (2017). Microtubules acquire resistance from mechanical breakage through intralumenal acetylation. Science *356*, 328–332.

Yadav, S., Verma, P.J., and Panda, D. (2014). C-terminal region of MAP7 domain containing protein 3 (MAP7D3) promotes microtubule polymerization by binding at the C-terminal tail of tubulin. PLoS One *9*, e99539.

Zanic, M., Widlund, P.O., Hyman, A.A., and Howard, J. (2013). Synergy between XMAP215 and EB1 increases microtubule growth rates to physiological levels. Nat. Cell Biol. *15*, 688–693.

Zehr, E.A., Szyk, A., Szczesna, E., and Roll-Mecak, A. (2020). Katanin grips the beta-tubulin tail through an electropositive double spiral to sever microtubules. Dev. Cell *52*, 118–131.e6.

Zhang, R., Alushin, G.M., Brown, A., and Nogales, E. (2015). Mechanistic origin of microtubule dynamic instability and its modulation by EB proteins. Cell *162*, 849–859.

Zhang, R., LaFrance, B., and Nogales, E. (2018). Separating the effects of nucleotide and EB binding on microtubule structure. Proc. Natl. Acad. Sci. USA *115*, E6191–E6200.

STAR★METHODS

KEY RESOURCES TABLE

REAGENT or RESOURCE	SOURCE	IDENTIFIER
Bacterial and virus strains		
E. coli BL21(DE3) CodonPlus-RIL competent cells	Agilent	Cat#230245
E. coli BL21(DE3) pLysS competent cells	ThermoFisher	Cat#606010
Chemicals, peptides, and recombinant proteins		
Recombinant human tubulin α1A/βIII	(Vemu, et al., 2016)	N/A
Recombinant human tubulin α1A-Y/βIII	This study	N/A
Recombinant human tubulin α1A-Δ2/βIII	This study	N/A
Recombinant human tubulin α1A-Δtail/βIII	This study	N/A
Recombinant human CLIP-170 H2 fragment with C-terminal GFP tag	(Bieling, et al., 2008)	N/A
Recombinant full-length human EB1 with C-terminal GFP-His tag	(Petry, et al., 2011)	N/A
Recombinant full-length human EB1, non-tagged	(Dixit, et al., 2009)	N/A
Porcine brain tubulin	Cytoskeleton, Inc.	Cat#T238P
Biotin-labeled porcine brain tubulin	Cytoskeleton, Inc.	Cat#T333P
α1B/βI+βIVb tubulin purified from tsA201 cells	(Vemu, et al., 2017)	N/A
Experimental models: cell lines		
Sf9 insect cells	ThermoFisher	Cat#11496015
tsA201 cells	Millipore, Sigma	96121229-1VL
Oligonucleotides		
α1A/βIII with PreScission site before FLAG-tag: CCGAGGCCCAGGGACCCAAACTGGAGGTGCTG TTCCAGGGTCCCGGTGGTAGCGGAGGAGACTAC; GTAGTCTCCTCCGCTACCACCGGGACCCTGGAA CAGCACCTCCAGTTTGGGTCCCTGGGCCTCGG	This study	N/A
α1A-Y/βIII generated by QuikChange mutagenesis: GAAGAGGAGGGCGAAGAATGAAAGCTGTCGAGAAG; CTTCTCGACAGCTTTCATTCTTCGCCCTCCTCTTC	This study	N/A
α1A-Δ2/βIII generated by QuikChange mutagenesis: GGCGAAGAGGAGGGCGAATGAAAGCTGTCGAGA AGTACTAGAGG; CCTCTAGTACTTCTCGACAGCT TTCATTCGCCCTCCTCTTCGCC	This study	N/A
α1A-Δtail/βIII generated by insertion of a stop codon: GGCGTCGATAGCTAAGTGGAGGGCGAG; CTCGCC CTCCACTTAGCTATCGACGCC	This study	N/A
Recombinant DNA		
pFast™-Dual vector	ThermoFisher	Cat#10712024
H. sapiens tubulin α1A/βIII in pFast™-Dual	(Vemu, et al., 2016)	N/A
H. sapiens tubulin α1A-Y/βIII in pFast™-Dual	This study	N/A
H. sapiens tubulin α1A-Δ2/βIII in pFast™-Dual	This study	N/A
H. sapiens tubulin α1A-Δtail/βIII in pFast™-Dual	This study	N/A
H. sapiens CLIP-170 H2 construct in pETEM	Dr. Thomas Surrey, Francis Crick Institute	N/A
H. sapiens GFP-tagged full-length EB1 in pET28	Dr. Kevin Slep, UNC	N/A
H. sapiens full-length EB1 in pGEX6p2	Dr. Sabine Petry, Princeton	N/A

(*Continued on next page*)

Continued

REAGENT or RESOURCE	SOURCE	IDENTIFIER
Software and algorithms		
Fiji	(Schindelin, et al., 2012)	https://imagej.net/Fiji
MATLAB 2019b	MathWorks	N/A
Prism	Graphpad	N/A
Jalview	(Waterhouse, et al., 2009)	https://www.jalview.org/
ESPript3.0	(Robert and Gouet, 2014)	https://espript.ibcp.fr/ESPript/ESPript/
Modeller	(Webb and Sali, 2014)	https://salilab.org/modeller/
Propka	(Olsson, et al., 2011)	https://pypi.org
Dowser	(Morozenko and Stuchebrukhov, 2016)	N/A
GROMACS 5	(MacKerell, et al., 2004; MacKerell, et al., 1998)	https://www.gromacs.org/
Parrinello-Rahman algorithm	(Parrinello and Rahman, 1981)	N/A
PyMOL v.2.0	PyMOL by Schrodinger	https://pymol.org/2/
PLUMED 2.5 plugin for GROMACS	(Tribello, et al., 2014)	https://www.plumed.org/doc-v2.5/user-doc/html/index.html
MDTraj open library	(McGibbon, et al., 2015)	https://www.mdtraj.org/1.9.5/index.html
ProKSim	(Khruschev, et al., 2015)	N/A
MATLAB scripts for microtubule dynamic analysis and comet analysis	(Vemu, et al., 2017) This study	https://github.com/RollmecakLab

RESOURCE AVAILABILITY

Lead contact

Further information and requests for resources and reagents should be directed to and will be fulfilled by the lead contact, Antonina Roll-Mecak (antonina@mail.nih.gov).

Material availability

All plasmids and cell lines used in this study are available upon request from the authors.

Data and code availability

MATLAB scripts used in this study for microtubule dynamics analysis and CLIP-170 comet analysis are available on GitHub: https://github.com/RollmecakLab.

EXPERIMENTAL MODEL AND SUBJECT DETAILS

All recombinant human tubulin were expressed in Sf9 insect cells. The cells were cultured in Sf-900^{TM} III SFM media at 27 °C, 125 rpm for 48 hrs after infection. GFP-H2 was expressed in *E. coli* BL21(DE3) CodonPlus RIL cells. GFP- EB1 and unlabeled EB1 were expressed in *E. coli* BL21(DE3) pLysS cells. Unmodified human α1B/βI+βIVb tubulin was purified from tsA201 cells. The tsA201 cells were cultured in Freestyle293 supplemented with 2% FBS and 1xPenicillin/Streptomycin at 37 °C, 125 rpm, 8% CO_2, and 70% humidity.

METHOD DETAILS

Purification of recombinant tubulin isotypes

All tubulin variants were expressed using baculovirus and purified as described previously (Vemu et al., 2016). Briefly, codon optimized α1A with an internal His-tag in the acetylation loop and PreScission protease cleaveable FLAG-tag on βIII tubulin were custom synthesized by IDT^{TM} and cloned into a pFAST™-Dual vector. Tubulin variants, α1A-Y/βIII, α1AΔ2/βIII and α1AΔ-tail /βIII, were made using Quick change mutagenesis. To ensure no insect tubulin contamination, α1A with an internal His-tag and βIII with a C-terminal cleavable Flag tag was purified using a Ni-NTA column (Qiagen) and anti-flag G1 affinity resin (Gen Script). The tubulin was then purified by ion exchange chromatography using a Resource Q anion exchange column (GE Healthcare). Peak fractions were combined and buffer exchanged into BRB80 (80 mM PIPES, pH 6.8, 1 mM EGTA, 1 mM $MgCl_2$) supplemented with 20 μM GTP using a PD10 column (GE Healthcare). All tubulin variants were subjected to liquid chromatography electrospray ionization time of flight mass

spectrometry (LC-ESI-TOF MS) analysis and no posttranslational modifications or endogenous insect tubulin contaminants were detected. The dynamic parameters are consistent between different tubulin growths and preparations (Figures S1A and S1B).

Purification of GFP-H2 and EB1

The GFP-H2 construct was a gift from the Surrey lab. Expression and purification of GFP-H2 was carried out as described previously (Bieling, et al., 2008) with slight modifications. Briefly, His-tagged GFP-H2 was expressed in *E. coli* BL21(DE3) CodonPlus-RIL. Cells were induced with 1 mM IPTG for 5 h at 30 °C and lysed by using high-pressure homogenizer in ice-cold lysis buffer (50 mM KP_i, pH 7.5, 500 mM NaCl, 1 mM $MgCl_2$, 1 mM β-mercaptoethanol) with Roche protease inhibitors. Precleared lysate was loaded onto a Ni^{2+} -NTA column and eluted with lysis buffer containing 300 mM imidazole. GFP-H2 was then purified using GE Q Sepharose Fast Flow with a gradient elution (50 mM KP_i, pH 7.5, 0.1-1 M NaCl, 1 mM $MgCl_2$, 1 mM β-mercaptoethanol). Overnight TEV digestion at 4 °C removed the His-tag. GFP-H2 was then loaded onto a Ni^{2+} -NTA column again. The flow-through was collected and further purified on a GE HiLoad Superdex 200 column. Peak fractions were pooled, supplemented with glycerol to a final concentration of 16%, flash frozen in liquid nitrogen and stored at -80 °C.

The EB1-GFP and EB1 constructs were expressed and purified as described previously (Petry, et al., 2011; Dixit, et al., 2009). Briefly, the His-tagged GFP-EB1 was expressed in *E.coli* BL21(DE3) pLysS, purified with affinity chromatography (Ni-NTA), ion exchange chromatography (GE Q Sepharose FF) and followed by size-exclusion chromatography in 80 mM PIPES, pH6.8, 100 mM KCl, 1 mM $MgCl_2$, 1 mM EGTA, 0.1% β-mercaptoethanol (GE HiLoad Superdex 200). The unlabeled EB1 has a N-terminal GST-tag followed by a PreScission cleavage site. The protein was expressed in *E.coli* BL21(DE3) pLysS and purified using glutathione resin. The GST-tag was removed by PreScission protease and the protein was further purified by Q Sepharose ion exchange and buffer exchanged into 80 mM PIPES, pH6.8, 100 mM KCl, 1 mM $MgCl_2$, 1 mM EGTA, 0.1% β-mercaptoethanol.

In vitro microtubule dynamics assays

GMPCPP-stabilized microtubule seeds were prepared as described (Gell, et al., 2010) and immobilized in flow chambers using neutravidin. The final imaging buffer is BRB80 (80 mM PIPES, pH 6.8, 1 mM EGTA, 1 mM $MgCl_2$) supplemented with 1mM GTP, 0.1% methylcellulose 4,000 cP, 1% pluronic F-127 and 0.1 mg/ml casein. An objective heater (Bioptechs) was used to warm the chamber to 30 °C. All chambers were sealed and allowed to equilibrate on the microscope stage for 5 min prior to imaging. IRM images were acquired on a Nikon Eclipse Ti-E equipped with a Hamamatsu ORCA Flash4.0 V2 sCMOS camera every 5 s for 30 or 60 min. For depolymerization rate measurements, the frame rate used was 20 frames/s.

EB1 and CLIP170 *in vitro* tip-tracking

Biotin-labeled GMPCPP stabilized microtubule seeds were double cycled from porcine brain tubulin and immobilized using neutravidin. The final assay buffer contains BRB80 (80 mM PIPES, pH 6.8, 1 mM EGTA, 1 mM $MgCl_2$) supplemented with 95 mM KCl, 85 mM KAc, 0.1% methylcellulose 4000 mPa.S, 0.5% pluronic F-127, 100 μg/ml κ-casein, 1 mM β-mercaptoethanol, and oxygen scavengers (Bieling, et al., 2008). All assays were carried out at 30 °C. All microtubule CLIP-170 end tracking assays were carried out at 30 °C, in presence of 6 or 15 μM recombinant tubulin, 300 nM EB1 and 75 nM GFP-H2 unless otherwise specified. Synchronous TIRF/IRM imaging was performed on a Nikon Eclipse Ti-E equipped with a LED light source, 488-laser and EMCCD cameras (Andor) with an exposure time of 100 ms per frame. Images were collected at 1 frame per second for 10 min. To obtain microtubule dynamic parameters in the presence of EB1 or CLIP-170, IRM images were recorded every 5 second for 1 h on a sCMOS camera (Hamamatsu).

MD simulations

A detailed description of MD simulations is provided in (Fedorov, et al., 2019). Computational architecture and performance of the simulations was described in (Fedorov, et al., 2018). In order to investigate the intradimer interaction of the α-tubulin tail we generated molecular models of tubulin dimers or tetramers (two longitudinally attached dimers; Figure S3A) based on microtubule cryo-EM structures (PDB IDs 3j6f and 3j6e (Alushin, et al., 2014)). The non-hydrolyzable GTP analog (GMPCPP) in the 3j6e structures was converted into GTP as described previously (Fedorov, et al., 2019). Unresolved amino acid chains, including C-terminal α- and β-tubulin tails were added in all the models, using the Modeller software (Webb and Sali, 2014). α-tubulin tails have the following sequence: VEGEGEEEGEEY, β-tubulin tails have the ATADEQGEFEEEGEEDEA sequence. Ionizable amino acid residues were protonated with Propka software (Olsson, et al., 2011). Intrinsic cavities in tubulins were identified and solvated with Dowser software (Morozenko and Stuchebrukhov, 2016). Tubulin dynamics were simulated using the GROMACS 5 software package with the CHARMM27 force field (MacKerell, et al., 2004; MacKerell, et al., 1998) in a virtual cubic reaction volume with periodic boundary conditions. The reaction volume size was selected so that the distance from the protein surface to the nearest box boundary was at least 2 nm. The virtual reaction volume was filled with TIP3P water and K+ and Cl− ions of 100 mM total ionic strength and zero total system charge. Each tubulin system was subjected to an energy-minimization, employing the steepest descent algorithm and then to a two-step equilibration, described in (Fedorov, et al., 2019). The production simulation runs were carried out in the NPT ensemble at 300K, using the Parrinello-Rahman algorithm (Parrinello and Rahman, 1981) and the V-rescale thermostat. The particle mesh Ewald method was used to treat the long-range electrostatics. All-bond P-LINCS constraints and mass rescaling (partial transfer of mass from heavy atoms to bound hydrogens (Feenstra, et al., 1999)) allowed molecular dynamics simulations with a 4 fs time step. All simulations of whole tubulins were one-microsecond-long and sampled with 1 ns intervals for analysis. Pymol (The PyMOL Molecular Graphics System, Version 2.0 Schrödinger, LLC) was used for visualization.

Metadynamics simulations of α-tail interactions

For enhanced sampling, we carried out a 2 μs-long metadynamics simulation using the GROMACS 2019.4 augmented with the PLUMED 2.5 package (Tribello, et al., 2014). Molecular model of tubulin was constructed as described previously (Fedorov, et al., 2019), using the structure of undecorated GMPCPP microtubule (PDB ID 6dpu (Zhang, et al., 2018). The simulated system contained α-tubulin body and α-tubulin tail, surrounded by a 10.4 x 12.8 x 9.7 nm box, centered around the origin of the α-tubulin tail. Cα - atoms of the tubulin core were position restrained. MD simulations were carried out as described in the section above, with the exception that an additional Gaussian energy potential with 0.1 kT depth and 0.1 nm width was applied to the center of mass of Y451 residue (Figure S4A). The position of the potential was updated every 0.4 ps (100 MD computation steps). Simulation results were processed with a custom Python script to plot the volumes around α-tubulin core, where the maximal numbers of additional energy potentials were applied to the tip of the C-terminal tail throughout the simulation (Figures S4B and S4C).

QUANTIFICATION AND STATISTICAL ANALYSIS

Microtubule dynamics analysis

Microtubule dynamics parameters were measured in ImageJ as previously described (Vemu, et al., 2016). Briefly, kymographs were generated from IRM images and hand traced to obtain growth and depolymerization speeds from the slopes of the growing and depolymerizing microtubules. Catastrophe frequency is defined as the number of catastrophes observed divided by the total time the microtubule spent in the growth phase. Rescue frequency is defined as the number of rescues observed divided by the total time the microtubule spent in the depolymerization phase. Tubulin association rate (k_{on}), the tubulin dissociation rate (k_{off}) and critical concentration were calculated using the slope, X and Y intercepts, respectively, of a simple linear regression fit in Prism using the mean growth rates at different tubulin concentrations and assuming 1625 dimers per micron of microtubule (Walker et al., 1988; Oosawa, 1970). The error reported is the standard error of the fit.

EB1 and CLIP-170 plus-end tracking analysis

The fluorescence signal of microtubule plus-end comets was analyzed as previously described (Vemu, et al., 2017; Bieling, et al., 2007). First, kymographs of the growing microtubules were drawn in ImageJ. Next, a custom-written MATLAB script was used to identify the maximum intensity in each line of the kymograph. Then an exponential fit to the line profile covering 1.5 μm of the lattice and a Gaussian fit to the line profile extending 1.5 μm beyond the microtubule tip was performed. For all exponential and Gaussian fitting, $R^2 > 0.99$. All fitted comet profiles were aligned, binned and averaged. The averaged comet profile was then fitted to a single exponential fit from the comet peak to the end of the comet with an offset that represents the lattice intensity. These comet profiles were then plotted in Prism and background corrected by subtracting the minimum background value. The reported comet intensity is the averaged peak value with background correction, and the lattice intensity is the background-corrected offset value, determined by the exponential fitting of comet tail.

Analysis of α-tubulin tail dynamics in MD simulations

Residues belonging to the tubulin polymerization interface were defined as those located closer than 4.5 Å to any of the residues of the adjacent longitudinally attached tubulin subunit. The fraction of polymerization interface occluded by the α-tubulin tail was calculated as follows. First, we artificially cut out the α-tubulin tail from the simulated MD trajectory of the tubulin dimer and determined the total solvent accessible surface area (SASA) for all amino acids belonging to the polymerization interface, every 1 ns of the simulation. SASA was computed using the *shrake_rupley* function of the MDTraj open library (McGibbon, et al., 2015). Then we repeated the calculation of the total SASA for the amino acids belonging to the polymerization interface without removing the tail from the MD trajectory. The fraction of occluded SASA was then calculated as the ratio of the difference between SASA in the absence and in the presence of the α-tubulin tail to the total SASA for the polymerization interface. Contacts between the α-tubulin tail and tubulin body were characterized with a custom Python script which identifies and counts residues of the tubulin body that are within 4.5 Å from residues of the α-tubulin tail. Probabilities of contacts between the tail of α-tubulin and its body were calculated as the average fraction of contacts over the whole simulation time, based on two simulations with one tubulin dimer and three simulations with the longitudinally assembled tubulin dimers (only the minus-end proximal α-tubulins were considered for tetramers) (Figure S3A). The distribution of electrostatic potential on the tubulin surface was mapped in Pymol based on Poisson-Boltzmann calculations performed using the ProKSim software (Khruschev, et al., 2015).